J. Biophoton. **3**, No. 5–6, 385–407 (2010) / **DOI** 10.1002/jbio.200900087

Journal of BIOPHOTONICS

REVIEW ARTICLE

Scanning fiber endoscopy with highly flexible, 1 mm catheterscopes for wide-field, full-color imaging

Cameron M. Lee[1], *Christoph J. Engelbrecht*[2], *Timothy D. Soper*[1], *Fritjof Helmchen*[2], *and Eric J. Seibel*[*,1]

[1] University of Washington, Dept. of Mechanical Engineering, Stevens Way Box 352600, Seattle Washington 98195, USA
[2] University of Zurich, Dept. of Neurophysiology, Brain Research Institute, Switzerland

Received 2 December 2009, revised 3 March 2010, accepted 4 March 2010
Published online 25 March 2010

Key words: medical imaging, optical scanning, endoscopy, endomicroscopy, two-photon microscopy

In modern endoscopy, wide field of view and full color are considered necessary for navigating inside the body, inspecting tissue for disease and guiding interventions such as biopsy or surgery. Current flexible endoscope technologies suffer from reduced resolution when device diameter shrinks. Endoscopic procedures today, using coherent fiber-bundle technology on the scale of 1 mm, are performed with such poor image quality that the clinician's vision meets the criteria for legal blindness. Here, we review a new and versatile scanning fiber-imaging technology and describe its implementation for ultrathin and flexible endoscopy. This scanning fiber endoscope (SFE) or catheterscope enables high-quality, laser-based, video imaging for ultrathin clinical applications, while also providing new options for *in vivo* biological research of subsurface tissue and high resolution fluorescence imaging.

Looking into the imaging head of a 1.2 mm scanning fiber endoscope

1. Introduction to ultrathin flexible endoscopes

Medical imaging of internal organs can be categorized into two groups: (1) structure-based imaging, such as X-ray computed tomography (CT), magnetic resonance imaging (MRI), and ultrasound, which typically image at low spatiotemporal resolution (millimeters, seconds); and (2) surface-based imaging using optical endoscope technologies, which image at high spatiotemporal resolution (micrometers, milliseconds). Because endoscopic imaging requires direct visualization of internal organ surfaces, both illumination and detection elements must be ported through an often tortuous anatomical geometry to a region of interest. As such, the accessibility of internal organs is dictated by both the size and rigidity of the endoscope. For many applications, a smaller diameter and flexible endoscope is often preferred for reducing tissue trauma

* Corresponding author: e-mail: eseibel@u.washington.edu

WILEY InterScience DISCOVER SOMETHING GREAT

© 2010 by WILEY-VCH Verlag GmbH & Co. KGaA, Weinheim

and medication (sedation) to reduce pain experienced by the subject [1].

Conventional flexible endoscopes are approximately the same thickness as a human finger and are primarily designed for high-quality color imaging. Relatively wide field of view imaging (>70° FOV) is necessary for navigating the scope within the body, inspecting tissue, diagnosing disease, and guiding surgical interventions. Flexible endoscopy was ushered in by coherent fiberoptic bundles (CFB), which serve as bendable conduits for transmitting light between proximal and distal ends of the endoscope [2]. CFB technology is still in use today, but more modern incarnations often employ a proximal video camera for image capture and subsequent display on a video monitor. Most flexible endoscopes are comprised of miniature charge-coupled device (CCD) video chips that have been placed at the distal tip of the flexible shaft, using incoherent optical fiber bundles to deliver white-light diffuse illumination [3]. Although these approaches technically differ, they share a common design feature: every pixel in the video display is associated with an imaging element, be it an optical core in the CFB or sensor element in a miniature video chip.

To accommodate imaging within small vessels, lumens, and ducts within the human body, ultrathin endoscopes have been developed by reducing the overall device diameter. However, ultrathin endoscopes less than 3 mm in diameter suffer from reduced image quality using conventional imaging technology. Typically, the minimum center-to-center spacing of imaging elements is 3 μm, requiring over 3 mm in diameter to produce 1024 line images. Manufacturers offer a wide assortment of CFB sizes and lengths suitable for endoscopic use [4, 5]. However, the CFB glass is suited for illumination in the visible to infrared range [6, 7], but not for wide-field fluorescence imaging using UV excitation [8]. To achieve higher spatial resolution while sacrificing FOV, laser-beam scanning at the proximal end of the CFB is performed in a confocal geometry for fluorescence microscopy, endoscopic microscopy or endomicroscopy [8–11].

Despite the unique advantages offered by CFB endoscopes as a passive device, there are also a number of limitations. Physically, the CFB is semirigid as the optical fibers are typically fused into a single glass rod. Bending the CFB often leads to core fracture, creating dead pixels in the display. During a clinical procedure, unintended perforation is perceived as a serious problem with ultrathin, semirigid endoscopes [12]. The ability to control shaft rigidity down to extreme flexibility of guidewires and catheters is needed. By matching endoscope mechanical properties to those of the target organ, the risk of perforation by submillimeter diameter scopes can be avoided [13]. Leached CFB technologies contain a nonfused length between distal and proximal ends, and were developed to alleviate durability and flexibility issues. These leached fiber bundles do exhibit some superior mechanical properties, but 2× lower core density than CFB and higher cost deter their acceptance [14].

The most confounding limitation of CFBs is poor image quality due to the restricted number of imaging pixels and a honeycomb effect produced by nonimaging space between optical cores. Both high resolution and wide FOV are not possible (see Section 4.2). For example, a standard CFB of 30 000 optical fibers has a 3 μm center-to-center spacing across an active area of 0.75 mm diameter resulting in 250 pixels across the FOV. If the distal lens produces an imaging FOV of 75°, then the minimal angle of resolution is roughly 0.3° per pixel. The human eye has a minimum angle of resolution of 1 min of arc or 1/60° or 0.0167°. Typically the primary legal definition for blindness is 10× lower visual acuity than normal vision (20/200 in USA or 6/60 in Europe [15], see also http://en.wikipedia.org/wiki/Blindness), which translates to 0.167°. A 1 mm endoscope using a ring of illumination fibers around a standard 30 000 fiber bundle generates images below the limit of legal blindness. Visual acuity can be increased by restricting FOV and magnifying the image, accomplished by changing the lensing. Although subcellular resolution is achievable, the microscopic FOV greatly impedes the utility of the endoscope. Again, the legal definition of blindness is helpful because its secondary criterion is having a restricted FOV (<20°) even with average visual acuity. These optical and mechanical limitations of CFB devices explain, in large part, why ultrathin flexible endoscopes are only minimally sufficient and not routinely used for medical procedures. Albeit there is great potential for performing less-invasive procedures in previously inaccessible regions of the human body if limitations in image quality and endoscope flexibility can be overcome.

In this paper, we review developments in the field of endoscopy and endomicroscopy with comparisons to a new scanning fiber endoscope (SFE) technology we have invented for the purpose of enhancing the performance of ultrathin flexible endoscopes and catheterscopes [1, 16]. The SFE technology produces high-resolution, large-FOV images by active scanning of laser light instead of passive imaging from diffuse white-light illumination. Low-power red, green, and blue (RGB) laser light is combined at the proximal end of the SFE and conveyed to the distal end using a single-mode optical fiber in a coaxial configuration. A fiber scanner is located at the scope's distal tip of the endoscope concentric with the optical axis, which allows diffraction-limited focus through the central part of the lens. When the near-end of this single optical fiber is held by a small piezoelectric actuator, the cantilevered free end of

© 2010 by WILEY-VCH Verlag GmbH & Co. KGaA, Weinheim

this optical waveguide can be vibrated near its mechanical resonance. A less than ±0.4 mm in lateral free-end deflection amplitude of the central fiber can project scanned laser illumination to greater than 100°, full angle to achieve wide FOV. Detection of the laser light can be realized in various reflection mode geometries. In this paper several modes of light collection are explained (see Section 2.4), though emphasis is placed on the nonconfocal mode of operation, as this geometry allows for wide FOV and high-quality color imaging that is essential to endoscopy.

Following a detailed description of the SFE technology in Section 2, unique features are discussed in Section 3. Alternative emerging endoscope technologies are compared in Section 4 with detailed comparisons of the SFE to conventional CFB and camera-based endoscopes. Specific clinical and research applications of SFE to wide-field imaging and of *in vivo* fluorescence SFE microscopy are reviewed in Section 5. In the latter application, subsurface functional imaging of the rodent brain is accomplished using the versatile SFE in combination with higher numerical aperture (NA) optics to achieve submicrometer lateral resolution. To conclude this review, we examine how this SFE instrumentation can advance clinical endoscopy and biomedical research. It is possible that entirely new concepts will be embraced by the next generation of clinicians who routinely use ultrathin flexible endoscopes for minimally invasive medical procedures.

2. Scanning fiber endoscope (SFE)

SFE technology has been developed at the University of Washington for the purpose of providing high-quality laser-based imaging within an ultrathin and flexible endoscope [16–19]. To our knowledge, the concept of moving an optical fiber to produce 2D images with confocal sectioning and laser illumination was first proposed for endoscopic applications by Giniunas et al. [20] in 1993. The major advancement of the SFE is rapid scanning and generation of high-quality images using an amplitude-modulated resonating fiber. This technique is versatile, allowing advanced laser-based diagnostics and therapeutics to be image guided.

2.1. *Mechanically resonant fiber scanner*

The central component of the SFE technology is a single optical waveguide vibrated at mechanical resonance to scan RGB laser light onto the image plane. The resonant single-mode optical fiber is vibrated laterally using a custom tubular piezoelectric (PZT 5A) actuator in an ultracompact coaxial design (Figure 1). The lateral vibratory motion can be modeled as a cylindrical, base-excited cantilever with fixed-free boundary conditions as in Eq. (1) [21]. The cantilever diameter is either the standard 125 micrometer or 80 μm cladding diameter of a fused silica, single-mode optical fiber [1]. Different specialty fibers can be used for particular applications, such as hollow-core photonics crystal fibers (PCFs) for distortion-free femtosecond pulse delivery [18, 22, 23]. The cantilever length is the extension of the fiber beyond the distal end of the tubular piezoelectric actuator (tube piezo), which determines the resonant frequency. By electrically driving the tube piezo near the scanning fiber's fundamental mode of lateral resonance, the fiber tip motion experiences a mechanical gain of 100 to 200 [24]. Shaping the cross-sectional axial profile along this fiber-optic cantilever from a cylinder to a more complex

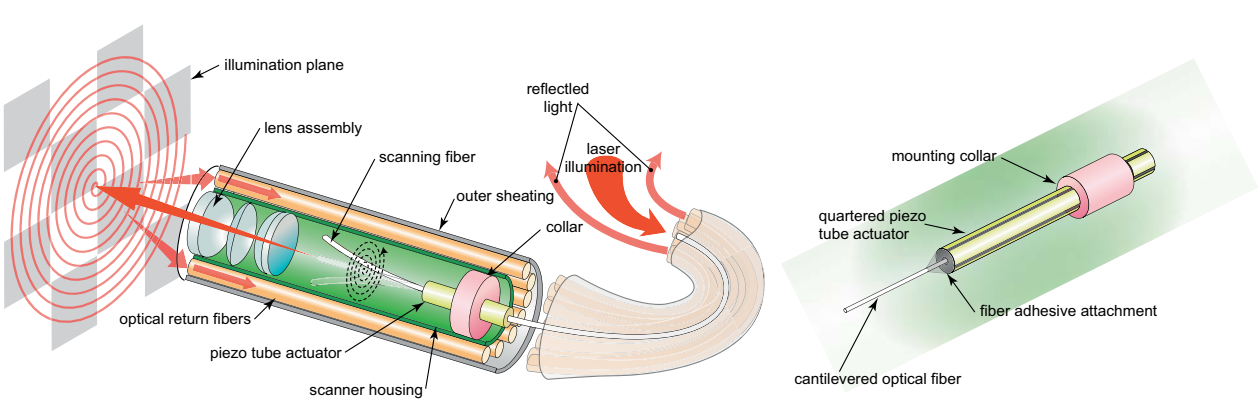

Figure 1 (online color at: www.biophotonics-journal.org) Functional diagram of the SFE with the scanning illumination fiber moving in the spiral scan pattern. A magnified view of the coaxial scanner design is shown, which consists of the central single-mode optical fiber that is cantilevered from the tip of a tubular piezoelectric actuator, held by a mounting collar.

© 2010 by WILEY-VCH Verlag GmbH & Co. KGaA, Weinheim

shape by acid etching can produce additional gains of 30% to 100% [25, 26]. Nonetheless, the general coaxial design of the SFE (Figure 1) is ideal for the compact and simple design of ultrathin endoscopes.

$$F = \frac{\pi\sqrt{E}}{16\sqrt{\varrho}}\frac{R}{L^2}\,(1.194^2, 2.988^2, \ldots) \quad (1)$$

In Eq. (1) describing the resonant frequency F, ϱ is the fiber density, E is the modulus of elasticity, R is the radius, and L is the length of the solid cylindrical fiber cantilever. Typical first-mode fiber resonance frequencies of 5 to 12 kHz are used for 1 mm catheterscopes with solid fused silica optical fibers of 125 to 80 µm in diameter, respectively. The mechanical resonance of the tube piezodriver can be ignored because the first resonant frequency of the short tubular structure is at least twice the first mechanical resonance of the fiber.

2.2. *Amplitude-modulated control of 2D resonant scanning*

Most resonant mechanical devices are operated at a fixed frequency and amplitude. The SFE operation is unconventional, as the optical fiber cantilever is rapidly excited and actively damped. Each video frame consists of three distinct phases: imaging, active breaking, and free decay (Figure 2). Each frame is captured by scanning the image plane in an outwardly growing spiral pattern. This spiral pattern is generated by applying increasing sine and cosine drive functions in the x and y image plane axes. Modest amounts of phase and amplitude adjustment are applied to the drive signal to optimize scan circularity. Upon completion of the spiral scan, an active breaking sequence drives the fiber back to its rest position by applying a high-amplitude drive signal that lags the fiber motion by 90°. This drive signal rapidly removes 95% of the scan motion in 5 to 30 cycles. Finally, actuation is halted, allowing the residual motion to decay naturally until the start of the next frame. Video imaging at 30 Hz and 500 lines per image is the standard scan setting. By changing

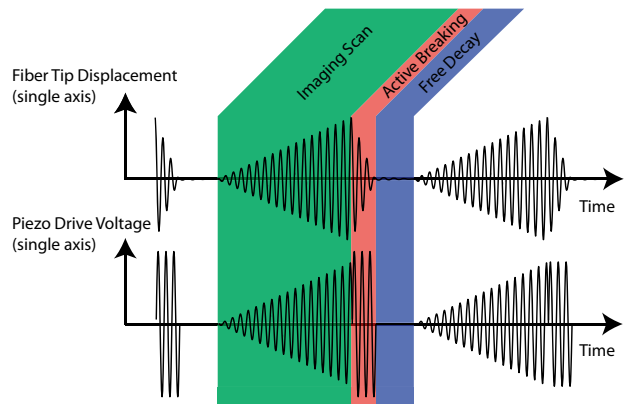

Figure 2 (online color at: www.biophotonics-journal.org) Electronic functional diagram of amplitude-modulated drive of the fiber scanner.

these parameters, alternative frame sizes, shapes, and durations can be achieved. For example, the standard 500 line images at 30 Hz frame rate can be changed to 1000 line images at 15 Hz for increased spatial resolution and reduced temporal resolution in the form of frame rate.

2.3. *Calibrating the fiber scanner for high image quality*

Closed-loop scanner feedback control is not required for maintaining high image quality for clinical applications. After the multilens assembly is aligned with the fiber scanner, the separation between fiber scanner tip and lens assembly determines the plane of sharpest focus. Typically, a low-NA endoscope lens assembly is used (Pentax, HOYA Corp.), resulting in a large depth of focus that is useful for resolving anatomical features over a large range of distances. The lenses can be adjusted during assembly to provide either 1–30 mm for small lumens or 2–60 mm for large lumens (Table 1). Other factors affect depth of focus, such as laser illumination power, number and size of collection fibers, sensitivity of light detection, and reflectivity of the object (tissue). The current SFE has laser powers of 1 mW blue

Table 1 1.2 mm SFE standard components.

Part (quantity)	Dimensions	Description
Tube piezo (1)	0.45 mm OD, 4 mm long	PZT5-A material
Drive electrodes (4)	5 µm thickness	Nickel plate material
Scan fiber (1)	0.080 mm OD, 2.27 mm long	Single-mode 0.13 NA 11 kHz res. freq
Lens assembly (1)	0.80 mm apertures OD	1–30 mm or 2–60 mm focal length, 100° FOV
Collection fibers (63)	0.050 mm OD	0.66 NA
Tip housing (1)	1.2 mm OD, 9 mm long	Stainless steel material
Flexible shaft (1)	1.2 mm OD, 1–4 m long	6 mm minimum bend radius

© 2010 by WILEY-VCH Verlag GmbH & Co. KGaA, Weinheim

(442 nm), 2 mW green (532 nm), and 2 mW red (635 nm) [18, 27]. Before initial use, the SFE probe is calibrated using a 2D position-sensing diode (UDT DLS-20) to maximize FOV, minimize scanner distortions, and provide white balance and chromatic compensation. A look-up table (LUT) can be used for each laser frequency to remap each point in the spiral scan pattern to a pixel position in rectilinear coordinates for electronic RGB digital display. In this way, sophisticated lateral chromatic aberration control is not necessary for the endoscope lens assembly. Each calibration setting is then stored as a file that can then be reloaded upon subsequent use, negating the need for future recalibration under normal operating conditions. Closed-loop temperature stabilization is important for any resonant scanner, especially for *in vivo* environs, where temperature changes occur as a result of contact with tissue, biological fluids (blood, mucus, etc.), and flushing fluids (saline, anesthetics, etc.).

2.4. Imaging modalities

In the standard SFE configuration, the RGB laser illumination is combined at the base station and coupled into the core of a single-mode optical fiber by a fiberoptic combiner or using free-space lenses and filters [18]. The resulting beam of RGB laser light is scanned and focused onto the image plane by a lens assembly that determines the maximum spatial resolution as defined by the point spread function (PSF). The standard (nonconfocal) geometry collects backscattered light with a ring of high-NA multimode optical fibers that surround the fiber scanner and lens assembly (Figure 1). The location, size, and number of these optical collection fibers determine the collection efficiency of the nonconfocal SFE. This standard nonconfocal geometry, which only uses the lens for illumination, is shown in Figure 3. Alternative SFE probe geometries are also shown, which include a dual illumination/collection lens configuration in a nonconfocal geometry for two-photon fluorescence [23, 28, 29] and confocal imaging for OCT [30]. Confocal geometries have the advantage of a smaller probe size, as a separate channel is not required for signal collection. However, the signal-collection efficiency of nonconfocal geometries is 40 times greater when collecting additional light from the inner cladding of a dual-clad optical fiber, especially at higher FOV [31, 32]. Due to the backreflections in typical endoscope objective lenses, inner-cladding detection is ideally suited for fluorescence imaging. A block diagram of the nonconfocal SFE system with concurrent fluorescence imaging in the near-infrared (NIR) is shown in Figure 4. In the future, it should be possible to combine two or more of these different signal collection geometries to increase signal-collection efficiency [33].

2.5. SFE as platform technology

The SFE may be considered a platform technology for flexible endoscopy because many different imaging modalities can be achieved using the fiber scanner. This submillimeter optical scanner could replace the CCD imager and illumination fibers if sufficiently cost effective for endoscope manufacturers. There is potential for high-volume mass production of the fiber scanner due to the simplicity of its design, which uses only a few low-cost components and may allow

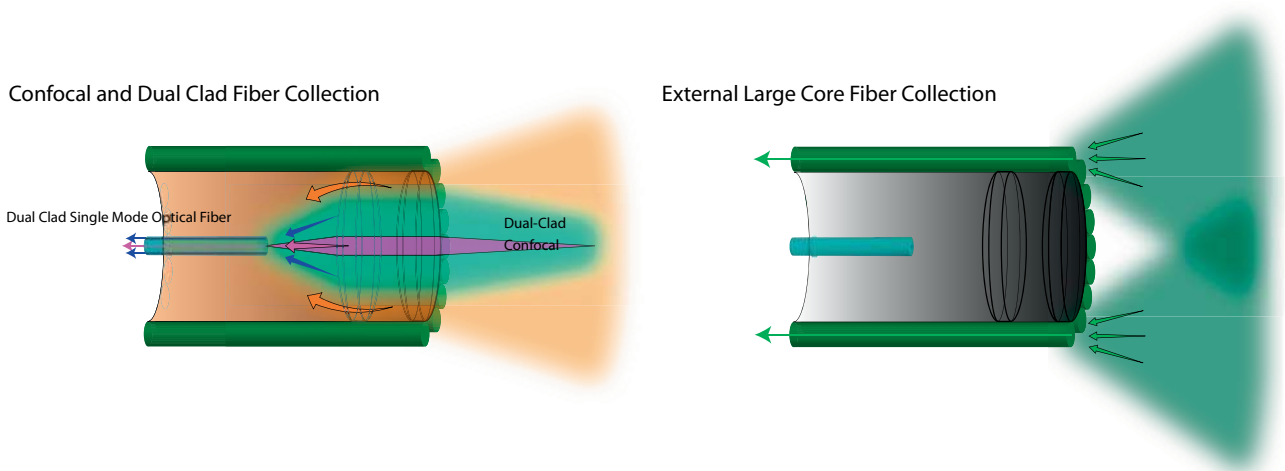

Figure 3 (online color at: www.biophotonics-journal.org) Optical collection methods: confocal, dual-clad and external large core fiber (non-confocal).

© 2010 by WILEY-VCH Verlag GmbH & Co. KGaA, Weinheim

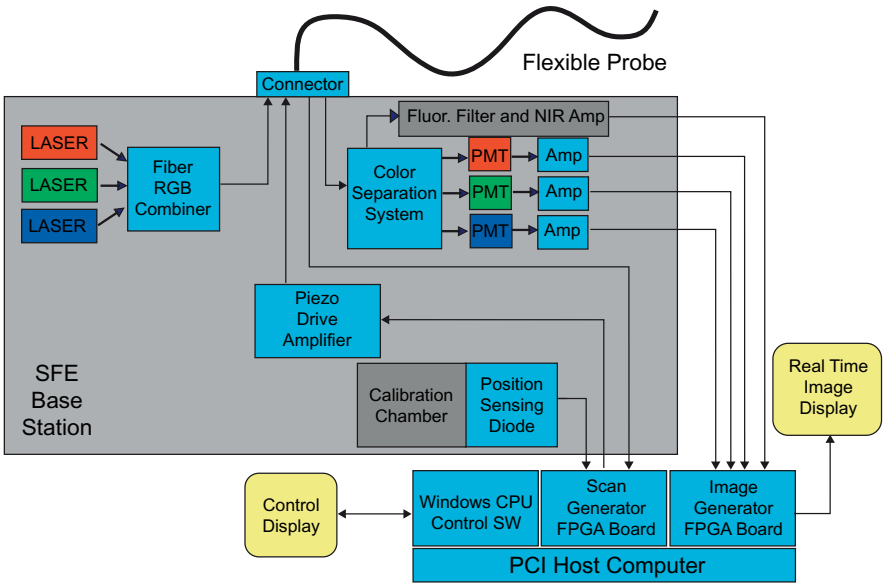

Figure 4 (online color at: www.biophotonics-journal.org) Block diagram of the SFE color system with 4th channel for near-infrared fluorescence.

for disposable use (Table 1). The choice of the distal lens assembly determines the optical properties of the endoscope, such as spatial resolution, FOV and depth of focus. However, even with a fixed resonant frequency and lens assembly, imaging parameters can be modified for the application. Versatility of each SFE probe is apparent in the adjustable scan settings: changing the realized FOV by varying the scan amplitude, changing image resolution by varying the number of scan lines per image frame, and adjusting image contrast by varying the individual laser outputs and detector gains for fluorescence imaging and image processing for enhanced spectral imaging.

In addition to the large number of scan settings that can be adjusted during normal operation of the SFE, a number of alternative imaging modalities can be integrated with slight modifications to the system. Table 2 contains a list of SFE imaging modalities. Items 1–6 are achieved with the standard embodiment, while 7–12 list alternative imaging modalities and the required design modifications.

3. Description of standard SFE features

Many features of the SFE technology were proposed in 2002 by Seibel and Smithwick [16] and over the past eight years nearly all have been demonstrated in proof-of-concept SFE systems by our group and others (Figure 5).

3.1. High resolution within 1 mm diameter

The SFE features that directly affect image resolution are the round coaxial geometry, high-resolution

Table 2 Listing of SFE features, 1–6 are standard and 7–12 require design modification.

#	Description of SFE feature
1	Full-color resolution (>500 lines) with high FOV (75°) with adjustable zoom and frame rate
2	Enhanced spectral imaging for improved tissue contrast
3	Fluorescence imaging capabilities
4	3D surface imaging
5	Spot optical spectroscopy at image center
6	Potential for disposable use of a sterile endoscope
7	Future laser therapies with dual-clad optical fiber
8	Additional illumination wavelengths (UV-NIR) using fused silica optical fiber
9	Confocal SFE achievable with spatial and chromatic filters and sensitive photodetector
10	OCT SFE achievable with low coherence source, reference arm and interference
11	Scanned two-photon fluorescence and second-harmonic generation with fs-pulse laser output, special fiber, and high-NA lens (see section 5.3)
12	Coherent anti-Stokes Raman scattering (CARS) SFE with ps-pulse laser outputs and moderate NA lens [122]

© 2010 by WILEY-VCH Verlag GmbH & Co. KGaA, Weinheim

Figure 5 (online color at: www.biophotonics-journal.org) Photograph of SFE system being used to image within a closed fist of the operator.

spiral scanning method and RGB single-mode laser illumination. Although coherent laser sources are often associated with interference effects such as speckle; consecutive pixels in the scanned field do not interfere with one another because of temporal separation. Furthermore, the large-area collectors in the nonconfocal geometry of the SFE help to mitigate any coherence effects by integrating high spatial frequencies. Thus, adverse interference effects can reasonably be avoided in most applications, and to this date have not been a limiting factor in any SFE application. In 1 mm diameter packages, the current implementation of the SFE provides over 6 times the image resolution of flexible CFB technologies and over 2 times the projected resolution of custom full-color silicon sensors. Additionally, the SFE has the ability to change FOV, resolution and frame rate during operation, allowing features such as electronic zoom and oversampling. A detailed discussion on resolutions, including basic assumptions and calculations is discussed in Sections 4.2–4.5 and summarized in Table 3.

3.2. Flexibility of shaft

The minimum short-term bend radius of a single glass optical fiber of approximately 0.1 mm in diameter is typically 5 to 6 mm (www.stokeryale.com; www.nufern.com). In the case of CFB, thousands of smaller-diameter optical fibers are rigidly combined to over 0.5 mm in diameter along the endoscope shaft so that the minimum bend radius escalates to centimeters with a concomitant high flexural rigidity. In comparison, the 1.2 mm SFE uses less than 70 loosely enclosed optical fibers within the shaft, thereby maintaining low flexural rigidity, and a minimum bend radius of roughly 6 mm. In both cases, flexural rigidity of the shaft must be increased to allow for pushability of the endoscope into the human body that can be achieved by adding wires, using thicker wall of sheathing, or using a more rigid insertion tube. In all SFE prototypes, length of the shaft is not a design limitation for deep explorations of the human body.

3.3. Scanner durability and safety

Any active device such as the electromechanical fiber scanner adds the theoretical risk that the moving part breaks and endoscope imaging ceases. A broken fiber does not affect patient safety as the fiber scanner is sealed within the endoscope tip with the lens assembly. During normal operation the laser power is less than 5 mW (equivalent to 3 laser pointers), which is less than standard endoscope illumination using arc-lamp sources. The electrical voltages applied during operation of the SFE are quite low as the tube piezo is electrically equivalent to a small capacitor. Typical operating voltages are less than ±20 V and electrical operating powers do not exceed 5.5 mW electrical power for video rate imaging at maximum FOV. In contrast, a CFB has no electrical requirement when the image capture device is at the proximal end outside the body. However, the CFB is considered mechani-

Table 3 Technology resolution comparison.

Device	System performance (532 nm)		Diffraction-limited performance (532 nm)	
	Pixel density pixels/mm^2	Image resolution pixels	Pixel density pixels/mm^2	Image resolution pixels in ∅ 0.85 mm
CFB	113 k	30.0 k/64.0 k$^{(1)}$	1.92 M	1.08 M
CCD/CMOS	238 k$^{(2)}$/476 k$^{(3)}$	95.0 k$^{(2)}$/190 k$^{(3)}$	1.92 M	1.08 M
SFE	345 k/496 k$^{(4,5)}$	196 k/282 k$^{(4)}$	1.92 M	1.08 M

(1) semirigid, (2) Bayer Filter, (3) sequential color, (4) 26 Hz frame rate, (5) virtual pixel density based on ∅ 0.85 mm sample area

© 2010 by WILEY-VCH Verlag GmbH & Co. KGaA, Weinheim

cally fragile in a clinical setting. The shaft of the SFE is highly flexible and added stiffness can provide a high degree of mechanical durability and added electrical insulation. In theory, the fiber scanner can break, but upon normal operation the single illumination fiber does not fatigue or fail, even when driven beyond the maximum 100° FOV for over 250 billion cycles in one test [1] and over 275 billion driven scan cycles in a subsequent test that continually scanned for over a year. No fiber wear has been observed in these lifetime tests. During routine use, prototype fiber scanner systems have stopped working, typically due to cracking of the adhesive joint between the fiber scanner and tube piezo. In drop testing of a fiber scanner at 2 m, the scanning illumination fiber never breaks, but sometimes the tube piezo cracks due to the high impact. Current SFE probes remain operational after repeated 1 m drop tests [1].

3.4. Depth imaging technologies

A minority of clinical practices rely on three-dimensional (3D) surface imaging, although emerging endoscopic fields of neurosurgery and robotic surgery are demanding stereoscopic image acquisition. Due to the small size of the SFE, stereo systems can simply be realized with two separate endoscope systems running synchronously, with one channel (left eye) imaging while the other channel (right eye) is retracing and resting with no laser illumination. Alternatively, the two SFE systems can run asynchronously with different filtration channels to maintain separation of the two overlapping image fields. Depth to the tissue surface and topography can be calculated in a SFE endoscopic system using photometric stereo algorithms [34]. This application of 3D imaging requires at least two or three separate views from the same SFE probe. Multiple views of the same object can be generated by the same fiber scanner by collecting and detecting the backscattered light separately, depending on the spatial location of the collection optical fibers located at the distal tip of the probe. For example, light collected from the left side of the probe will be shadowed more from a tissue protuberance on the left of the scanned illumination than the light collected from the right side of the probe. Depth can be determined by measuring the size of the specular reflection pattern and using the lever-arm analogy to estimate separation distance [35]. Subsurface tissue imaging is another form of 3D imaging but is limited to endomicroscopy techniques, such as confocal and optical coherence tomography (OCT), which is not covered in detail within this review.

3.5. Enhanced spectral imaging and multichannel fluorescence imaging

The SFE uses narrow bands of illumination light to produce full-color images of tissue at high fidelity on flat surfaces. However, within a body lumen that is predominantly red in color (esophagus), the user typically reduces the gain on the red channel to pro-

(a) (b) (c)

Figure 6 (online color at: www.biophotonics-journal.org) SFE bronchoscopic image frames from standard RGB imaging at 500-line images at 30 Hz (**a**) and the corresponding ESI image (**b**) that increases contrast of blue laser light over the red laser light, helping to differentiate blood vessels and inflamed tissue. SFE fluorescence image acquired on the red channel showing hypericin localization within a tumor of renal cell carcinoma (**c**). Blue and green laser illumination was used, while a small fraction of the blue backscattered light was collected to form the background structural image.

© 2010 by WILEY-VCH Verlag GmbH & Co. KGaA, Weinheim

duce more-balanced color images. A recent innovation by Olympus has eliminated the red within the filtered white-light imaging of conventional endoscopes for the purpose of enhancing blood-vessel patterns within the subsurface tissue that are associated with cancer and other diseases [36]. For example, capillary networks in the surface mucosa can be imaged at higher contrast. Although tissue color is distorted, this form of enhanced spectral imaging (ESI) can be a standard feature of the SFE either during endoscopy or upon postprocessing for computer-aided diagnosis [37]. Figure 6a depicts an endobronchial image within the airways of a live pig that is processed in Figure 6b to accentuate blood vessels and damaged tissue.

Wide-field fluorescence imaging is also a standard feature of the SFE technology. For biomarkers used for photodynamic therapy (PDT) and photodynamic detection (PDD) that have wide excitation spectra, such as 5-ALA and hypericin [38], the RGB laser illumination can be used for both reflectance imaging and PDD/PDT applications. A proof-of-concept experiment was performed by perfusing hypericin into the vasculature of a rat kidney with renal cell carcinoma *in situ* and SFE fluorescence imaging on the red channel provided the cancer-specific image overlaid onto the structural image provided by the backscattered signal from the blue excitation light (Figure 6c) [39]. If a fourth detection channel is added for the deep-red fluorescence imaging for such dyes as Cy5 (Figure 4), then fluorescence can be imaged concurrently with full-color (RGB) reflectance imaging. A fifth channel is often desired for subtracting the background signal from nonspecific biomarker labeling for more clinical utility [40]. Again, the narrow laser bands for excitation lend itself to multichannel fluorescence imaging either concurrently with RGB imaging or in a frame-sequential manner.

3.6. Integrated spot diagnosis and therapy with imaging

Between every imaging frame, the scanning fiber is brought to rest at the central pixel for microseconds to milliseconds for fluorescence spectral analysis of extrinsic biomarkers [41]. However, the duration of this rest phase can be lengthened to allow time for applications that require longer dwell times of laser illumination, such as laser-induced fluorescence spectroscopy of intrinsic biomarkers [19] (Figure 7). In cancer diagnosis, endoscopy is performed to locate suspicious tissue for biopsy (cell and tissue samples for cytology and pathology) [37]. Typically, the clinician steers the endoscope so

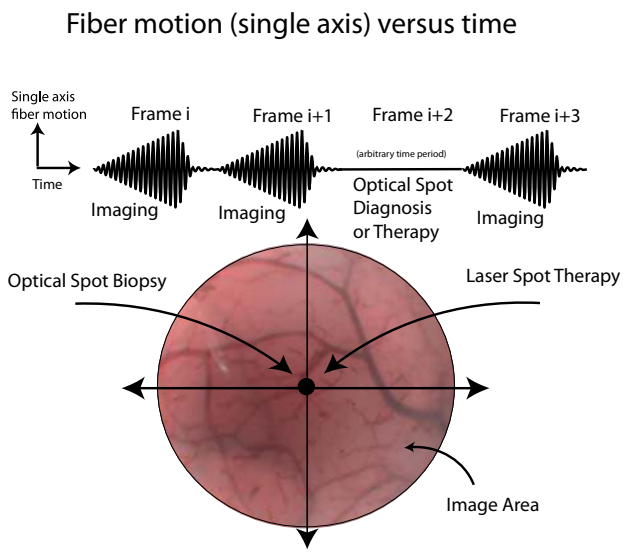

Figure 7 (online color at: www.biophotonics-journal.org) Frame-sequential imaging, diagnosis or therapy.

the site location for biopsy is within the endoscope's FOV for image-guided sampling. Performing a noninvasive optical biopsy at this location prior to a real biopsy will give greater assurance that only the most suspicious tissues are being removed for further analysis. Optical spot biopsy has already been developed and tested for many different technologies in cancer detection, such as light-scattering spectroscopy, laser-induced fluorescence spectroscopy, fluorescence lifetime analysis, and Raman spectroscopy [42–45]. Video imaging can be interrupted for the exact time needed to complete this optical diagnosis and resumed immediately after, thereby combining imaging and diagnosis in a frame sequential manner.

For highly efficient fluorescence microspheres, a spectrum of both laser excitation and fluorescence emission can be acquired within 3 ms using the standard SFE with tip bending (Figure 8) [41]. Thus, spectral analysis is possible during the fiber resting phase between SFE video image frames at 30 Hz. If these interruptions in SFE video imaging are brief, then frame-sequential imaging, therapy, and monitoring are possible in the future. Laser-spot destruction of tissue would be possible under near real-time monitoring in a frame-sequential imaging mode [46]. Alternatively, therapeutic drugs may be photoactively released with a pulse of extended dwell time [47]. Since small, solid-core single-mode illumination fibers are restrictive in laser power delivery, a dual-clad optical fiber may be used for conveying higher laser power to the tissue. During the rest phase, the fiber delivers therapeutic laser power through the inner cladding, and during the scanning phase the fiber delivers imaging RGB illumination

© 2010 by WILEY-VCH Verlag GmbH & Co. KGaA, Weinheim

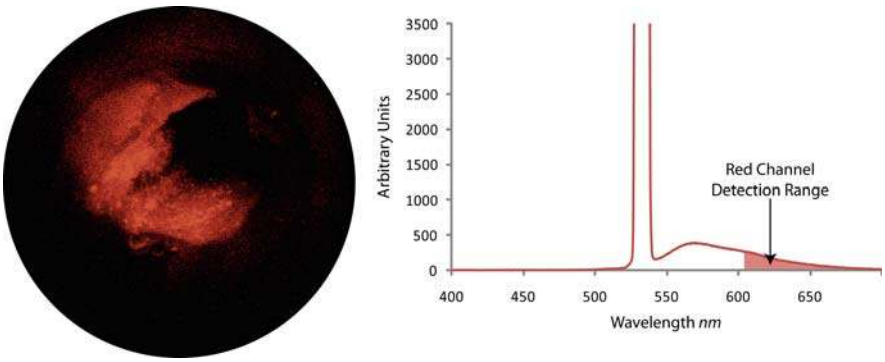

Figure 8 (online color at: www.biophotonics-journal.org) SFE video frame (left) of fluorescence microspheres (Nile-red FluoSphere, F-8819, Molecular Probes) embedded within a synthetic phantom of a bile duct. Optical spectral analysis (right) that shows the high laser illumination at 532 nm and fluorescence emission when collection optical fibers are connected to a spectrometer (USB2000-FL, Ocean Optics). SFE red-channel detection range is illustrated on the spectral plot.

through the single-mode core. By hand scanning the endoscope tip, the pulsing high-power spot is slowly moved over the tissue while an image frame is generated by rapidly scanning low-power RGB light between therapeutic pulses. Thus, imaging and therapy are multiplexed in a frame-sequential time series allowing near real-time monitoring.

3.7. Summary of SFE features

The SFE technology allows a great variety of standard features to the clinician. Topics not discussed as part of the central design include active tip bending [48] and *in vivo* tracking of the distal tip using electromagnetic sensors [49, 50]. In the first half of Table 2, the basic features are listed for the standard (nonconfocal) SFE imaging at video frame rates. With modifications to the standard SFE components and probe geometry, a wide range of nonstandard features are possible, as listed in the second half of Table 2.

4. Ultrathin endoscopic technologies under development

The limitations of the CFB technology have been apparent to medical device engineers for the past twenty years, driving a number of alternative technologies that are surveyed in this section. The general clinical approaches have been improving upon the CFB, such as adding laser-scanning confocal imaging to improve spatial resolution and stitching multiple images into larger mosaics to overcome FOV limitations of confocal endomicroscopy (Mauna Kea Technologies, Paris, France) [51, 52]. Although the CFBs have been used for imaging at high spatial resolutions via proximal-end laser scanning [9, 10], the resulting *in vivo* confocal fluorescence microscopes provide only submillimeter FOV, thus restricting broad clinical utility. Consequently, the trend in clinical endoscopy has been to slowly replace fiberoptic systems with more expensive custom video chips at the endoscope tip [53, 54]. The major flexible endoscope manufacturers (Olympus, Pentax, and Fujinon, all headquartered in Japan) have been placing a custom video-chip camera at the endoscope distal end and expanding the image contrast by filtering the illumination light to include fluorescence and narrowband image processing. A wireless video-chip camera with LED illumination is being used in the development of capsule endoscopes, such as Given Imaging, which uses a complementary metal oxide semiconductor (CMOS) sensor [55] and Olympus, which uses a CCD [56].

4.1. Alternative scanning approaches to endoscopy

The newest technological approaches to high-resolution imaging employ a microscanner placed at the distal tip of the endoscope. Most commonly, optical scanning is performed using a moving mirror in a confocal optical geometry using microelectromechanical systems (MEMS) [57–62]. However, to achieve subcellular spatial resolutions, FOV must be sacrificed, hindering broad clinical utility. A wide-FOV MEMS endoscopic device has been designed using a 0.5 mm scan mirror, however, the packaging enlarges the device size to greater than 2 mm [63]. Unique circumferential line scanning has been demonstrated using a dual-reflectance large scan MEMS mirror, but again the device footprint is $2 \times 2\ \mathrm{mm}^2$ [64]. Smaller device diameters are theoretically possible using the scanning of a MEMS cantilever originally proposed by Dickensheets and Kino [65] for a confocal geo-

© 2010 by WILEY-VCH Verlag GmbH & Co. KGaA, Weinheim

metry and by Wang et al. [66] in a nonconfocal geometry. Ultimately, MEMS designs have not translated to the commercial market, possibly as a result of high fabrication setup costs and limited application given the small FOV and relatively large diameters. A clinical solution, demonstrated by Kiesslich et al. [67], performed *in vivo* confocal imaging by scanning an optical fiber driven by an electromechanical motor. Though commercially available from Pentax, this 3D high-resolution imaging is housed within endoscope diameters greater than 10 mm that produces FOVs smaller than 1 mm.

Since MEMS optical scan systems tend to be much larger than 1 mm in diameter, alternative scanning strategies have been investigated with the goal of maintaining ultrathin device diameters. In a previous study, a 1 mm catheter has been rotated axially to scan a single beam in a 360° radial path [68]. The concept of rotational scanning was later extended to two dimensions using a line of near-infrared light generated from polychromatic illumination passing through a grating [69]. This spectrally encoded endoscopy technique has been shown to generate images beneath tissue surfaces using 860–880 nm light by increasing sensitivity [70]. Recently, a bench-top version of this system has incorporated color imaging in the visible spectrum [71]. This same concept of using dispersion of broadband laser to spectrally encode and decode spatial information has been extended to 2D without the need for any mechanical scan system [72]. Again, this system has been proposed for endoscopy from a bench-top demonstration, but as a confocal system with limited FOV in the infrared spectrum [73]. These new technologies are very promising for miniaturization into ultrathin endoscopes. However, the requirement of polychromatic laser wavelengths interacting with dispersion elements in the visible spectrum in lieu of wide-field mechanical scanning may pose a significant technical challenge to translation into routine clinical use. Currently, the best clinical alternative to 2D scanning is rotation of a side-viewing endoscope while axially moving the scope within the lumen, albeit slowly, while generating 360° radial images [74].

4.2. Wide-field endoscopic imaging limitations

The complication with producing high resolution in ultrathin flexible endoscopes is producing devices that are capable of effectively fitting and operating in the highly confined device. CFB and CCD technology used in modern endoscopes today, fail to take full advantage of the 1-mm area afforded inside the endoscope and as a result, produce less than optimal image quality. CFBs have remained the mainstay in small flexible scopes and provide sufficient sampling resolution in many applications. However, the low mechanical flexibility of the CFB deters the use of high core count bundles. For this reason, custom CCD and emerging CMOS image sensors have strong potential to replace their glass counterpart, promising higher resolutions and better mechanical properties. However, expense and technical complication surrounding color, packaging and electronic characteristics, prevent their immediate adoption. Unlike traditional endoscope detectors, the flexible single-mode fiber and coaxial scanning design of the SFE, take full advantage of the cylindrical space using spiral scan patterns that fill the entirety of the lens system.

The resolution considerations of CFB, CCD/CMOS, and SFE are described in more detail for the 1-mm size in the following sections (4.3–4.5). For comparative review, these results are tabulated in Table 3. In comparing imaging performance, other parameters are important for ultrasmall imagers, such as dynamic range, signal-to-noise, and cross-talk, but will not be reviewed in order to retain some brevity. Before examining the details of current and future SFE technologies, a brief description of CFB, CCD and CMOS technologies is offered. CFB devices are used to transfer the image from the distal to proximal end of the endoscope by passively relaying light through a series of spatially aligned optical conduits. Either an eyepiece or video camera attachment captures images at the proximal end of the device. CCD and CMOS sensors are used to capture images at the distal end of the flexible endoscope and relay image electrical signals from the device. The basic photoconversion process of these two silicon devices is similar but their readout operations differ. Both CCD and CMOS technologies utilize an array of small photodiodes to capture spatial and intensity data. CCD pixels utilize a shifting mechanism that allows pixel charge to be transferred between adjacent pixels. In video full-frame transfer CCDs (FT-CCD) the pixel charge is first shifted off the pixels to a buffer and then read out individually by a charge-to-voltage converter. CMOS sensors use a small transistor element for each pixel element, converting charge to voltage locally. A row- and column-addressing scheme is used to address and read from each pixel.

4.3. CFB resolution considerations

Today, most ultrathin endoscopes use small coherent fiber bundles that contain several thousand tightly packed optical cores (Figure 9). The spatial sampling

© 2010 by WILEY-VCH Verlag GmbH & Co. KGaA, Weinheim

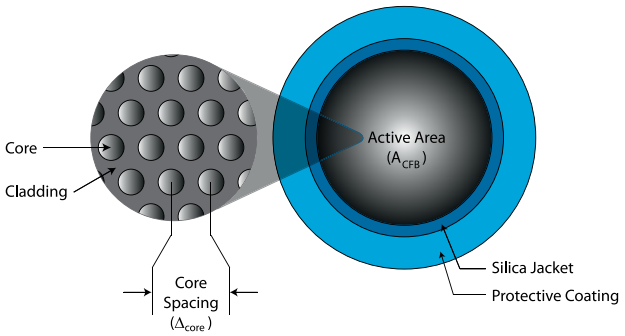

Figure 9 (online color at: www.biophotonics-journal.org) Fused coherent fiber bundle (CFB) cross-sectional view.

period of these CFBs is determined by core size and spacing [75]; however, cross-coupling effects between cores can reduce their effective sampling characteristics [76]. Cross-coupling effects can be mitigated by providing adequate core separation, but this strategy can become counterproductive if applied too liberally. In small-core systems, the core-separation distance becomes a significant factor when determining the sampling characteristics of the device.

Commercial coherent fiber bundles are manufactured with cores diameters of 2 μm and core separation (Δ_{core}) as small as 3.2 μm [4, 5, 8]. Typical CFBs have a silica jacket and protective coating that combined take up a nominal 150 μm of the total diameter. Based on 60° alignment of cores, basic geometry can be applied to calculate a cross-sectional core density of 113k cores/mm^2 in these CFBs (Eq. (2)).

By assuming the entire cross-sectional area in a ∅ 1 mm device could be fitted with the CFB, a prorated active area A_{CFB} of 0.567 mm^2 remains after accounting for space lost from the jacket and sheath. A display resolution of 64 k pixels can be calculated from core density and active area (Eq. (3)). Unfortunately, the implications of using such a thick CFB would cause the endoscope to have a cumbersome minimum bend radius of nearly 5 cm [4, 5]. For this reason, small endoscope designs tend to use thinner CFBs yielding resolutions between 10–30 k pixels [6]. Alternatively, a bare 30 k fiber bundle is used for combined illumination and imaging that results in reduced pixel numbers (<100 across the FOV) and leads to fragility during clinical procedures [77, 78].

$$\text{Core density} = \frac{2}{\sqrt{3}}\left(\frac{1}{\Delta_{\text{core}}}\right)^2 \tag{2}$$

$$\text{Image resolution} = (\text{core density})\,(A_{\text{cfb}}) \tag{3}$$

For many years CFBs were used exclusively in flexible endoscopy, but their low durability and high rigidity were undesirable. The typical CFB endoscope suffers continual degradation of image quality over its lifetime, losing pixels from core fractures within the bundle. Eventually, the degradation becomes so severe that the device is no longer suitable for use. Leached CFBs have solved some of the original durability issues, but with core spacing of 2.5 to 3 times of that in nonleached CFBs, their resolution is not yet competitive [14]. Since the inception of the CCD video scope, the CFB endoscope has slowly lost popularity. Small-diameter endoscopes are one of the last applications where the CFB excels over the CCD. High pixel density, small form factor and low cost make the CFB sufficient for many ultrathin endoscope applications.

4.4 CCD/CMOS resolution considerations

Continuing improvement in CMOS and CCD sensor miniaturization, fueled by the commercial market for mobile phone and pc camera application, suggests the silicon sensor may soon overtake the CFB. State-of-the-art research in silicon sensors has demonstrated 16 × 16 frame transfer CCD arrays with pixel element sizes as small as 0.5 μm × 0.5 μm [79]. More functional 3.0 M pixel CMOS sensors with 1.45 μm pixel size [80] and 3.1 M pixel FT-CCDs with 1.56 μm pixel size [81] have been successfully developed. This suggests that commercial silicon sensors may be capable of sampling beyond the diffraction limit of a camera-lens system.

In practice, several factors have prevented the silicon sensor from realizing the full potential of these small pixel sizes. The rectangular geometry associated with standard wafer-cutting techniques limits the usable sensor area inside a cylindrical casing (Figure 10). Further loss is also experienced because the entire dye cannot be used for active sensing. Typically, over 50% of the sensor dye space is used for wire-bond points, keep-out area and supporting functionality such as frame buffers, pixel addressing and signal amplifiers. Additionally, complications including blooming, cross-talk, low dynamic range, and poor light collection surround further pixel-size reduction [3, 82, 83].

In addition to geometric limitations, color information comes at a cost. With the exception of the triple-well active pixel sensor developed by Foveon [84] or frame sequential color [53], at least three different sensor elements are needed per color sample. A mosaic pattern of red, green and blue pixel sensors, referred to as the Bayer filter, is the most universal method for detecting color on a single chip [85]. This method reduces the fundamental linear sample frequency for red and blue to 50% and green to 70.7% of the pixel pitch. Because green is closely linked to our perception of luminance and spatial frequency, sampling effects of red and blue are less important. It has been suggested that resolution of a

© 2010 by WILEY-VCH Verlag GmbH & Co. KGaA, Weinheim

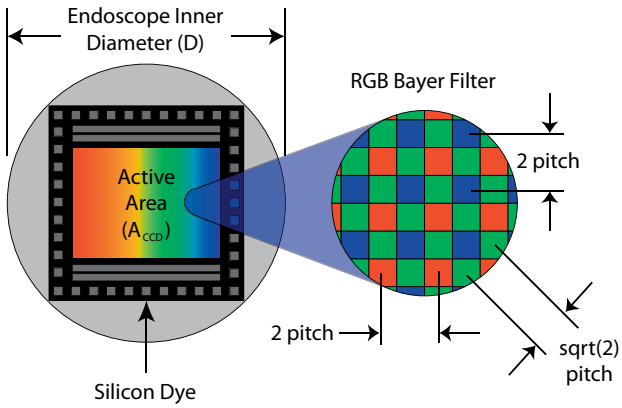

Figure 10 (online color at: www.biophotonics-journal.org) CCD and CMOS Illustration.

sensor using RGB sensing pixel element (Foveon) is as effective as a sensor twice to three times the area using a Bayer filter [86].

At this point, there are no known commercial CCD or CMOS devices that are capable of fitting in a 1 mm diameter scope ($D = 1$), but for comparison purposes we will consider highly specialized silicon sensor. Based on a 1.45 µm pixel pitch (Δ pixel) and 80% dye utilization (DU) such a sensor would capture 190 k pixels images; however, after prorating the resolution affect associated with the Bayer filter only 63.4–95.1 k effective color pixels would be resolved.

$$A_{\mathrm{ccd}} = (\mathrm{DU})\left(\frac{D^2}{2}\right) \tag{4}$$

$$\text{Monochrome image resolution} = \left(\frac{A_{\mathrm{ccd}}}{\Delta^2_{\mathrm{pixel}}}\right) \tag{5}$$

From the resolution projections calculated from Eqs. (4) and (5) it appears that silicon sensor resolution is superior to the CFB; however, these projected resolution numbers do not take into account higher-order effects or manufacturing complications. It has been shown that decreasing pixel size can adversely affect resolution when there is low illumination and induced camera motion, suggesting that slightly larger pixel elements more practical [82].

4.5 SFE resolution considerations

The SFE sample resolution, unlike CCD, CMOS or CFB technology, is not fixed by the physical size and spacing of pixel elements. Instead the scanning motion and sampling rate determine the sample spacing. Because neither of these parameters is fixed during fabrication, the device resolution, scan angle and frame rate are readily adjustable. In practice, mechanical properties limit the number of reasonable scan patterns that can be produced. These producible scan patterns generally exhibit nonuniform sampling and retrace that reduce their effective pixel count and frame rate. In addition, scan behavior is also subject to distortion caused by nonideal dynamic system behavior and actuator limitations. Although real-time closed-loop control methods have been used to reduce scan error, the space limitations of clinical devices preclude the use of bulky position sensing diode sensors [87]. With improved construction techniques, scanning systems today exhibit highly repeatable scan patterns, making open-loop methods a viable solution [18, 88].

The 11 kHz microscanner in the SFE produces 250 radially increasing spirals followed by a nominal 20–30 active breaking cycles and 50–60 free decay cycles. The entire scan process has a period of 1/30th of a second. At the sample rate is 25 MSps a total of 625 000 samples are captured and mapped to circular image with effective display resolution to 196 k pixels [1]. Similarly, the scan pattern has been run at slightly reduced frame rates of 26 Hz allowing for an additional 50 image spirals. This modified scan captures a total of 750 000 samples that map to an effective display resolution of 282 k pixels. In summary the SFE in its current incarnation is capable of significantly higher sampling then CFB, CCD and CMOS in 1 mm devices and it is capable of adjusting frame rate and resolution (Table 3).

Although sensor limitation can be used to differentiate the SFE from CFB, CCD and CMOS technologies, all flexible endoscope designs are limited by the diffraction of light (Figure 11). The spatial point spread function (PSF) imparted on the image is determined by both the objective lens and the illumination properties. In endoscopes, this PSF has the largest effect at the real focal plane inside the device. The limited area within the device and the resolvable separation between points can be used to calculate the image resolution in this wide FOV application. Rayleigh (Eq. (7)) and Sparrow (Eq. (8)))

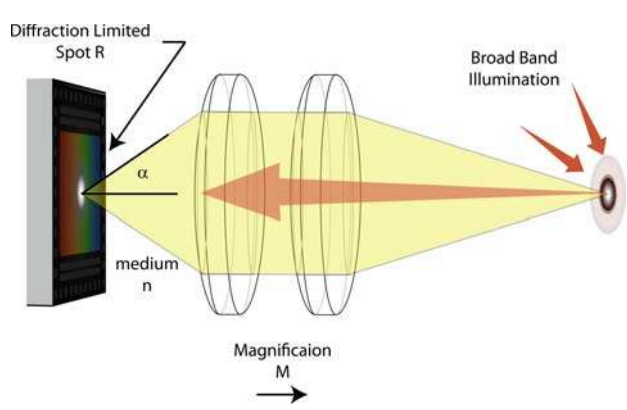

Figure 11 (online color at: www.biophotonics-journal.org) Traditional endoscope optics.

© 2010 by WILEY-VCH Verlag GmbH & Co. KGaA, Weinheim

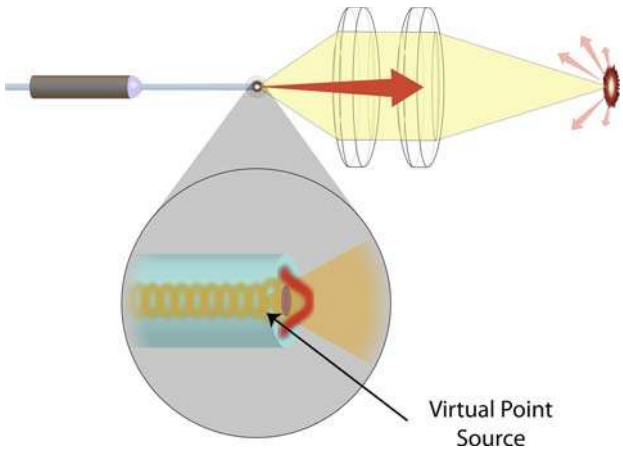

Figure 12 (online color at: www.biophotonics-journal.org) SFE optics.

resolution criteria can be used to quantify the minimum resolvable separation between points, where NA indicated the numerical aperture lens and λ the illumination wavelength. The NA of the objective can be quantified using Eq. (6) relating the convergence angle α and the index of refraction n, of the medium inside the scope. For calculation purposes, the Sparrow criterion is used, because it is based on human perceptual factors and can be applied to a variety of PSFs including Airy disk and Gaussian beam [89].

$$\mathrm{NA} = n \cdot \sin(\alpha) \tag{6}$$

$$\text{Rayleigh} = \frac{1.22\lambda}{\mathrm{NA}} \tag{7}$$

$$\text{Sparrow} = \frac{0.95\lambda}{\mathrm{NA}} \tag{8}$$

For a fully illuminated objective, with NA of 0.35 and central wavelength of 53 nm, 479 k points can be resolved per square mm using the Sparrow criterion. At minimum Nyquist sampling, this equates to approximately, 1.92 M pixels/mm^2, or 1.08 M pixels on a ∅ 0.85 mm diameter area behind the lens. The SFE has the unique capability of sampling at the lens limitations because a virtual point source is formed at the tip of the fiber when the coherent light exits the single-mode core (Figure 12) [90]. Assuming there are negligible aberration effects, this point source is capable of realizing the diffraction limited PSF.

In previous studies, this sampling characteristic of the SFE has been used to perform electronic zooming by reducing fiber deflection to narrow the FOV (Figure 13). This equates to higher angular resolution up to the optical limitations of the lens. Although, in this particular case, oversampling was used to achieve a zoom effect, in conjunction with deconvolution algorithms, enhanced spatial resolution is possible.

5. SFE applications

The SFE technology has been tested *in vivo* in large lumens organs of the human upper digestive tract (esophagus and stomach) down to small lumens within pig airways and bile duct. With an optical window at the lens distal end, the SFE images equally well in air or liquid.

5.1. Tethered capsule endoscope (TCE) in esophagus

The first clinical application of the SFE was in the form of self-experimentation of the principle investigator using a swallowable version, called the tethered capsule endoscope (TCE) (Figure 14) [27]. The larger TCE probe is shown in relation to the 1.2 mm diameter SFE in Figures 14a and b. Parallel to the 1.4 mm tether of the TCE is an air channel to allow for insufflations of the esophagus to facilitate imaging of the first healthy subjects without any adverse effects [91]. The ability to insufflate allows for rapid imaging of the gastroesophageal junction in unsedated patients because bubbles can be quickly removed from the FOV and the pressure can trigger the opening of this junction in order to detect inflammation and Barrett's esophagus, a precancerous condition. While standard TCE imaging is similar to white-light imaging, the RGB laser sources allows for postimaging processing akin to commercially available narrowband imaging [92] in order to improve visualization of mucosal detail [37, 91] (Figures 14c and d). While wireless capsule endoscopy is currently available to image the esophagus, this technique does not allow for insufflations of the esophageal lumen, nor is control of the imaging field by the

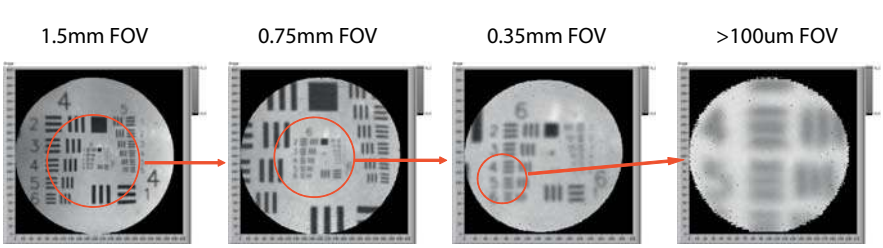

Figure 13 (online color at: www.biophotonics-journal.org) Scan adaption for electronic zoom.

© 2010 by WILEY-VCH Verlag GmbH & Co. KGaA, Weinheim

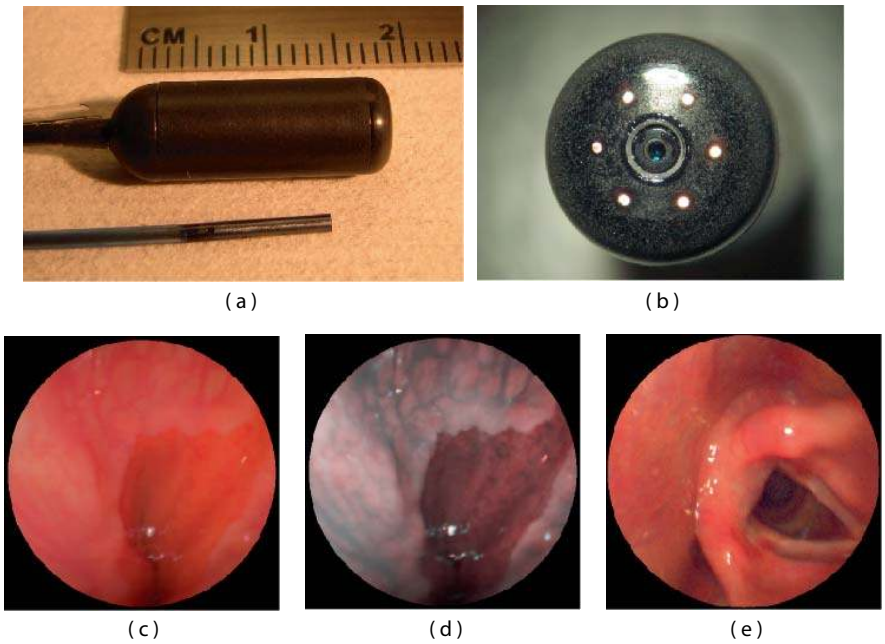

Figure 14 (online color at: www.biophotonics-journal.org) SFE endoscope probes showing 9 mm rigid tip length of 1.2 mm diameter prototype and 18 mm capsule length of 6.4 mm diameter TCE. A front view of the distal end of the TCE is shown in (**b**) illustrating that the TCE is a standard SFE probe with collection fibers modified for capsule use. The gastroesophageal junction of a human subject is shown in single 500-line RGB image contrast (**c**) compared to postprocessed ESI contrast of the same SFE image frame (**d**). The lighter esophageal tissue is more clearly differentiated from the red-colored gastric mucosa in the ESI image. An image of the human vocal chords is shown in (**e**).

endoscopist possible as illustrated in the vocal chord image (Figure 14e). Untethered capsule endoscopy has shown no clear advantage over conventional endoscopy [93]. However, tying a string on the wireless capsule endoscope to allow for reusability and physician control like the TCE has shown higher performance and lower cost than conventional endoscopy [94]. Laser-based imaging in combination with image processing for comprehensive surveillance of the esophagus has been demonstrated for 3D-OCT monochrome analysis [95] and for 2D-TCE color analysis [27]. A future goal is to reliably detect high-grade dysplasia in Barrett's esophagus [96] with a combination of SFE technologies, such as wide-field fluorescence imaging and mosaicing [97].

5.2. *SFE in airways*

The first *in vivo* experiment using the SFE was performed to examine the airways of a live pig. The SFE is particularly relevant to bronchoscopy given the incidence of lung cancer, need for improved diagnostic instruments, and the small lumen sizes being accessed. At present, computed tomography (CT) scans indicate the presence of numerous pulmonary nodules within patients suspected of having lung cancer. However, due to the invasive nature of surgically resecting such nodules and the potential loss of lung function, intervention is reserved for patients in whom a malignant diagnosis is highly suspect. Biopsy of a nodule provides the best chance at accurate diagnosis. Bronchoscopy is considered to be the most minimally invasive of biopsy procedures, but the accuracy of the procedure is inhibited by the inability to extend conventional bronchoscopes into small airways where these nodules occur. However, the accessible lung volume afforded by the small SFE is significantly greater. Whereas conventional bronchoscopes, with an outer diameter of approximately 6 mm (Figure 15a), are limited to the first four airway generations (2^4 or 16 airways), the SFE is capable of insertion through 8 to 10 branching generations, amounting to several hundred or thousand airways.

SFE-based examination of these peripheral nodules is highly practical. First, patients identified with lesions would be able to undergo bronchoscopy for a more definitive diagnosis. This would obviate more-invasive transthoracic biopsy procedures as well as the repeated CT scanning performed as part of ongoing surveillance of nodules not deemed large enough to merit initial intervention. Using the SFE, bronchoscopy can be performed without the need of expensive imaging systems and surgical suites, and can be used in conjunction with conventional bronchoscopes through the 2.4 mm working channel.

Figure 15b compares bronchoscopic images of the airways in a live pig acquired from both a conventional Pentax bronchoscope and the SFE. The resolution and field of view of the two devices are comparable despite a four-fold reduction in size of the SFE. The color discrepancy is due to the illumination sources; conventional bronchoscopes use an arc-lamp, while the SFE uses red, green, and blue laser diodes. The conventional bronchoscope is not capable of extending much further than the third- or fourth-generation airways. However, the SFE could be extended a number of generations further into peripheral airways.

© 2010 by WILEY-VCH Verlag GmbH & Co. KGaA, Weinheim

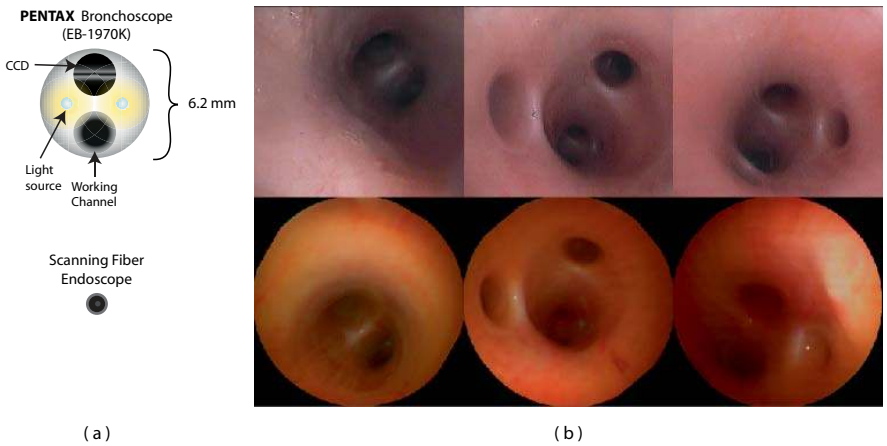

Figure 15 (online color at: www.biophotonics-journal.org) Diagrams of a conventional Pentax bronchoscope (EB-1970K) and SFE (**a**) and corresponding bronchoscopic images within the airways of a pig.

In practical consideration of implementing the SFE as part of a complete bronchoscopic system, a number of additional features are being incorporated for image-guided bronchoscopy. First, a steering mechanism is being constructed to permit articulation of the SFE (Figure 16a). A large bend angle of 90° and small bend radius (6 mm) will allow the SFE to negotiate sharp bend angles to access upper airway regions (Figure 16b). To assist the bronchoscopist in navigating multiple airway generations, a virtual guidance system has been developed to track the position of the SFE [49, 50]. Intraoperative localization is achieved through integration of a miniature (0.30 mm) electromagnetic position sensor (Ascension Technology Corporation, Burlington, VT) that can be used to locate the SFE in 3D space (Figure 16c). Custom biopsy tools have been proposed that are introduced over the SFE that is a steered and tracked catheterscope, such as a cannula-style tube for lavage, a brush for cytological sampling and a cutting needle for tissue biopsy [98].

5.3. SFE in biomedical research

In addition to endoscopic imaging for clinical diagnosis and treatment, miniaturized fiber-optic imaging devices such as the SFE also open up new ways for microscopy studies in biomedical research fields like neuroscience. Overviews of different ongoing technological developments in this area can be found in [99–102]. In neuroscience the development of miniature, lightweight fiber-optic microscopes [23, 60, 75, 103–106] is leading towards two long-standing goals of cellular-resolution brain imaging: First, endoscopic approaches promise to enable high-resolution imaging from deep brain areas, which are otherwise inaccessible for optical analysis. Secondly, small portable microscopes will permit measurements of the neural dynamics underlying specific behaviors in awake, freely moving animals, thus overcoming the limitations of current in vivo experiments under anesthesia that suffer from alterations in neuronal and astrocytic activities.

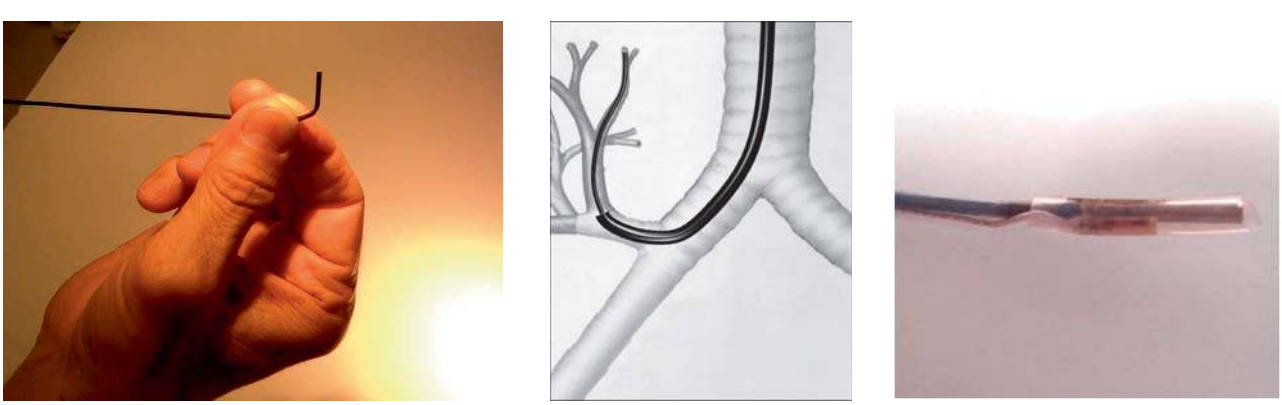

Figure 16 (online color at: www.biophotonics-journal.org) Additional features are incorporated into the SFE design to permit bronchoscopic examination of small peripheral airways include: a steering mechanism (**a**) and guidance system that is used to locate SFE by means of a miniature (0.30 mm) sensor.

© 2010 by WILEY-VCH Verlag GmbH & Co. KGaA, Weinheim

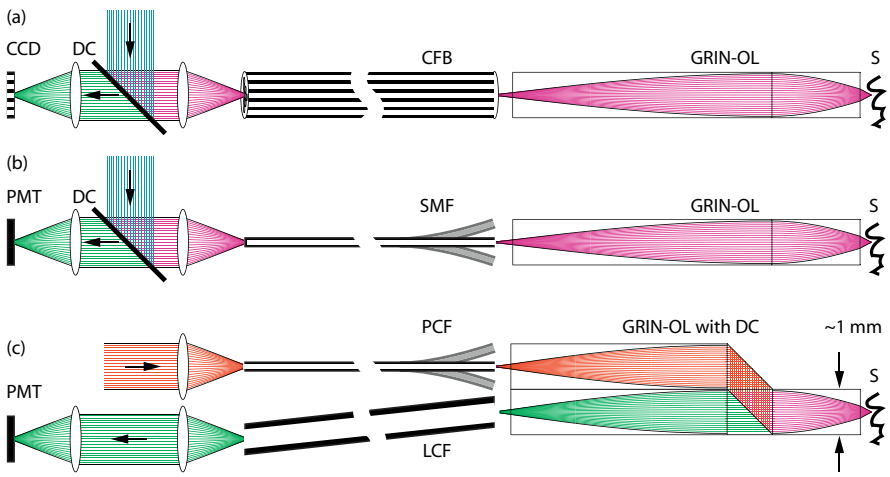

Figure 17 (online color at: www.biophotonics-journal.org) Fundamental overview of different fiberscope types used in biomedical research. (**a**) CFB-based fiberscope, usually implemented as single-photon excitation wide-field type. An image of the sample S is propagated through the gradient-index objective lens GRIN-OL and the coherent fiber-bundle CFB and remotely detected using a CCD-chip behind a dichroic beam splitter DC (green rays). Fluorescence excitation light travels to the sample in the reverse direction (blue rays). In principle, this type can also be used in combination with proximal (on the optical table) beam scanning for single- and two-photon excitation microscopy. (**b**) Scanning-type fiberscope, usually implemented as single-photon or two-photon excitation microscope. Fluorescence excitation light (blue rays) is guided to the distal fiberscope headpiece via DC and through a single-mode fiber SMF and is focused onto S via GRIN-OL. Fluorescence emission light (green rays) is usually proximally detected by a photomultiplier tube PMT after traveling the reverse direction. Distal beam scanning is usually achieved by either resonant fiber scanners, or MEMS scanners. Fluorescence-detection efficiencies can be improved with dual-clad fibers. (**c**) Scanning-type fiberscope, usually implemented as two-photon excitation fiberscope. Dichroic beam splitting occurs distally in a custom microprism arrangement that is part of GRIN-OL. Near-infrared fluorescence excitation photons (red rays) are guided through a photonic crystal fiber PCF that permits distortion-free delivery of femtosecond pulses. Fluorescence emission photons from S are remotely detected by a PMT after traveling through a large-core fiber LCF for improved efficiencies.

Unlike the catheterscopes described above that allow imaging with large FOVs, neuroscientific applications aim at micrometer-resolution imaging of individual cells. As a consequence, different front lens systems with high NAs are required, which, however, limit the FOV to a few hundred micrometers. In principle, single-photon or two-photon fluorescence excitation modes can be used, both featuring certain advantages and disadvantages (Figure 17). Miniature microscopes have been realized as either wide-field CFB-type or scanning-type fiberscopes. In the latter case scanning is performed either at the proximal end of a CFB [75] or at the distal end with a single-mode fiber scanner [18, 23, 103, 104]. Recently, the construction of a portable CFB-type fiberscope has enabled investigators to visualize blood flow in hippocampus and to measure neuronal calcium dynamics in cerebellar Purkinje cell dendrites in freely moving mice [105]. Advantages of the single-photon CFB approach are fast acquisition rates (usually only limited by the camera speed), relatively large FOVs, and mechanical simplicity and rigidity. Disadvantages include limited optical penetration depths due to strong light scattering in neural tissue, increased background fluorescence levels, decreased contrast levels, and potentially high photobleaching rates due to out-of-focus excitation.

In two-photon microscopy [107] reduced scattering at longer wavelengths, spatial localization of fluorescence excitation, and low phototoxicity lead to distinct advantages for deep-tissue imaging [108, 109]. The development of miniaturized two-photon fiberscopes has therefore gained particular interest in brain research. Two-photon fiberscopes typically utilize 100 fs pulses of near-infrared light for fluorescence excitation. Because of the group velocity dispersion introduced by the fiber material as well as nonlinear effects at high intensities these pulses are broadened several-fold in standard single-mode fibers, reducing the efficiency of two-photon excitation. This problem can be alleviated or circumvented, however, by using special photonic crystal fibers (PCFs) for efficient pulse delivery [22, 23, 104, 110, 111]. Moreover, various fiber-scanning approaches have been implemented including resonant fiber vibrations [23, 103, 104], fiber-tip deflection [112], and microelectromechanical systems with small mirrors [60, 106, 113, 114]. The laser output from the scanning fiber tip typically is imaged through a gradient-index (GRIN) lens objective [9, 23, 75, 104, 115], while fluorescence emission is col-

© 2010 by WILEY-VCH Verlag GmbH & Co. KGaA, Weinheim

lected through a second large-core optical fiber [23] or a dual-clad fiber [29, 116, 117], or is detected with a small photodetector integrated in the fiberscope front piece [103, 118]. Most technological approaches so far have used GRIN lenses with moderate NAs in the range of 0.5. Therefore, theses systems were able to resolve fluorescent structures in the micrometer regime but were outperformed by standard, higher-NA two-photon microscopes. Newly developed GRIN-assemblies can have NAs of up to 0.85 and therefore exhibit even higher optical resolution and better light collection efficiencies [106, 119]. However, application of these high-NA systems in miniaturized microscopes is still pending. The formation of lenses on the fiber tip itself [120] might be an interesting alternative for further miniaturization attempts, albeit at the cost of decreased NAs.

Using the SFE technology in combination with a specialized hollow-core PCF [22] we constructed an ultracompact (0.6 g) fiber-optic two-photon microscope [23]. Laser pulses from a Ti:sapphire laser system were coupled into the hollow-core PCF and guided to the microscope headpiece with minimal group velocity dispersion (GVD). The tip of the illumination fiber was resonantly vibrating in a spiral trajectory, which was then imaged onto the sample by a 1 mm diameter GRIN-lens assembly consisting of collimator, beam splitter, objective lens, and detection fiber coupler as described in Figure 17. Fluorescence emission was guided through the objective lens, beam splitter, fiber coupler, detection fiber, and remotely detected by a photomultiplier tube (PMT). The PMT-current signal was amplified and digitized by a multifunction data acquisition (DAQ) board and fluorescence intensity values were assigned to their corresponding pixels based on a static lookup-table (LUT). Optionally, image distortions can be corrected for by remapping pixels, applying a previously measured LUT using the same procedures as described above. Achievable FOVs were 200 μm in diameter. Frame rates critically depended on the spiral parameters used for imaging with typical values being video-rate (25 Hz) before averaging. Lateral and axial spatial resolutions (full widths at half-maximum, FWHM) were measured to be 0.98 ± 0.09 μm and 7.68 ± 1.30 μm, respectively, with subresolution fluorescent microspheres. Using this device we could demonstrate the instrument's suitability for functional calcium imaging of neuronal activity in the intact brain of an anesthetized rat (Figure 18). With a slightly larger two-photon fiberscope another group recently succeeded in imaging single-cell activity in the visual cortex of freely moving rats [121] indicating that high-resolution calcium-imaging studies in freely behaving animals with miniaturized two-photon microscopes are imminent.

Future versions of SFE-based miniature fluorescence microscopes could benefit from high-NA GRIN lens assemblies leading to higher resolutions and better light collection efficiencies. Furthermore, elongated thin front lens systems may allow imaging of deeper brain structures and readout of neuronal activity patterns. Finally, optimized driving and fiber-braking schemes could improve frame rates as well as spiral stability. Overall, the combination of novel fluorescent probes (e.g. fluorescent protein expression in transgenic animals) with the highly flexible SFE technology promises to reveal detailed information about fundamental physiological processes as they occur in the living animal.

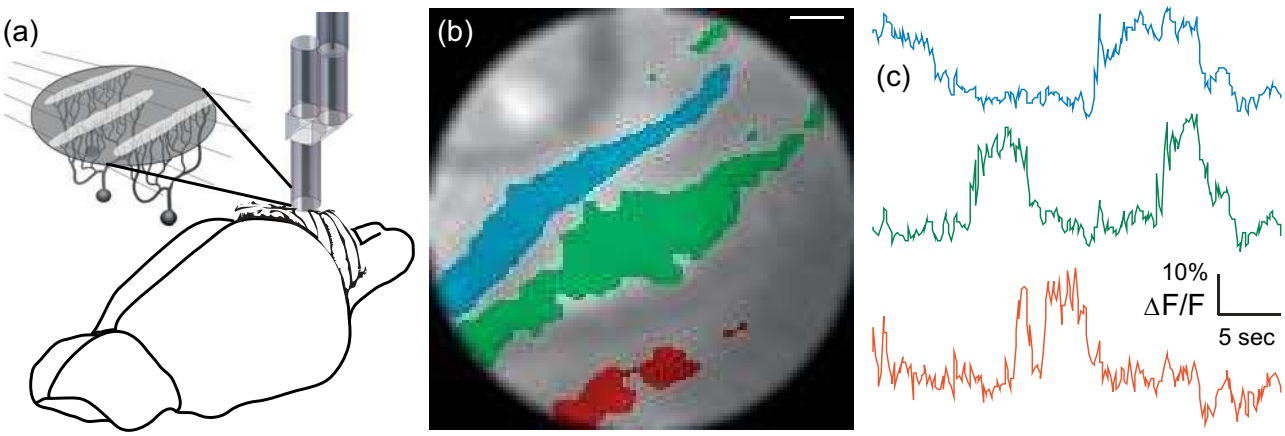

Figure 18 (online color at: www.biophotonics-journal.org) Fiberscope data acquired from rat cerebellum. (**a**) Anatomical organization of the rat cerebellar cortex. Flat dendritic trees of Purkinje cells form parasagittal planes that appear as band-like structures when observed from above. (**b**) Region-of-interest (ROI) selection (colored areas) can be a semiautomated process based on independent component analysis (ICA). (**c**) Spontaneous $\Delta F/F$ traces that are color coded to match the ROI selections in (**b**). Scale bar is 15 μm. Reproduced with permission from [23].

© 2010 by WILEY-VCH Verlag GmbH & Co. KGaA, Weinheim

6. Conclusions and future directions

High-performance ultrathin endoscopes and catheterscopes are the technological basis for image-guided medical procedures deep within the body, often with unsedated patients, which lowers risk and cost. In the future, soft and flexible endoscopes may be quasi-implantable so that more chronic conditions can be monitored through longer-term dynamic monitoring. Furthermore, the ultrathin size of the SFE allows insertion into the body through a 16-gauge needle, which is no longer considered surgery as anesthesia and suturing is no longer required. The catheterscope is essentially a guidewire with eyes, over which cannula-style tools can be introduced for cell sampling and biopsy. Similar to interventional cardiology, the SFE catheter and associated tools may be sufficiently low in cost to be disposable and device sterility can be assured.

The microlaser scanning of the SFE technology allows many of the most advanced microscopic techniques developed for *in vitro* analysis to now be conducted *in vivo*. An analogous transition has already occurred in many research laboratories, switching from wide-field optical microscopy to laser scanning microscopy for diagnostic imaging and laser dissection. By using active laser scanning, the catheterscope can be used for integrated imaging, diagnosis, therapy, and monitoring in a frame-sequential basis. Since a vast majority of cancers originate in the epithelium layer, laser biomarker diagnostics may be the preferred approach to identify and diagnose the earliest cancers. Using pixel-level control of the laser sources, the SFE technology can then be used to destroy these early cancers *in situ* with minimal healthy tissue damage. The laser-based catheterscope is assisted by the growing use of fluorescence biomarkers and gold nanoparticles with molecular-specific binding to disease for integrated diagnosis and treatment. As reviewed here, the SFE technology provides the affordance of new directions and concepts in clinical medicine and basic medical research.

Acknowledgements Current and past clinical collaborators with Dr. Seibel, especially: Drs. J. Dominitz, R. Yeung, M. Saunders, R. Glenny, D. Haynor, S. Park, J. Chien, T. Brentnall, M. Kimmey, and M. Sinanan. All members of the Human Photonics Lab and past members of the Human Interface Technology Lab who have contributed in great and small to this project: R. Johnston, C. Melville, M. Kundrat, D. Gertler, W. Yoon, C. Brown, Q. Smithwick, E. Barhoum, M. Fauver, J. Myers, J. Crossman-Bosworth, M. Kirshenbaum, B. Murray and T. Furness. However, this research would not have been possible without the expertise in design, development, and analysis from C. D. Melville, R. S. Johnston, and P. G. Reinhall. Current funding is from NIBIB (R01008119 and RC1EB010900), NCI (U54 CA136429 (Wang), and CA 128231 (Dominitz)), and the W. H. Coulter Foundation. Past support that developed this technology came from The Whitaker Foundation, Washington Technology Center, NSF CBET 0809070, NIH/NCI (R21 CA110184, R21/R33 CA094303) and PENTAX (HOYA Corporation) with special appreciation to Dr. H. Baker, Mr. T. Hidaka, and Mr. T. Shimada. Research support in the Helmchen lab was from the Human Frontier Science Program, the Swiss National Center for Competence in Research "Neural Plasticity and Repair", and the EU-FP7 program (project 200873).

Cameron Lee received his bachelor's degree and master's degree in Electrical Engineering at the University of Washington. For the past six years to present, he has worked for the Human Photonics Lab designing custom electronics, photo detection systems, DSP algorithms and dedicated image processing hardware. His ultimate goal is to develop technologies that will progress beyond the confines of the research lab and prove beneficial to the public.

Christoph Engelbrecht received his "Diplom" in physics from the Ruprecht-Karls-University Heidelberg, Germany. In his diploma thesis at the European Molecular Biology Laboratory (EMBL), he worked on the development and characterization of novel fluorescence microscopy techniques in the biosciences. Chris recently finished his doctoral thesis in physics at the Swiss Federal Institute of Technology Zurich, Switzerland (ETH Zurich). Most of his thesis work was carried out at the Brain Research Institute, University Zurich, involving a close collaboration with the Seibel lab at the University of Washington. Other research interests include simulations, designs, implementations, and characterizations of various microscopy techniques.

© 2010 by WILEY-VCH Verlag GmbH & Co. KGaA, Weinheim

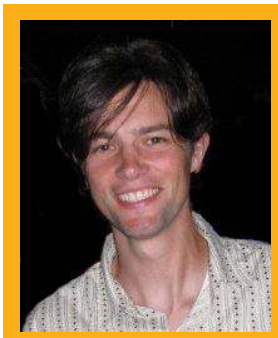

Timothy Soper received his bachelor's degree in bioengineering from the University of California, San Diego and doctoral degree from the University of Washington in bioengineering. Currently, he researches endoscopic tracking algorithms at the Human Photonics Laboratory at UW and is part of a development team to produce a clinical system for bronchoscopic evaluation of peripheral lung lesions. Other research interests include deformable image registration, airway segmentation, and user interface development for medical applications.

Fritjof Helmchen received his master degree in Physics from the University of Heidelberg, Germany. He completed his Ph.D. thesis in Neuroscience at the Max-Planck-Institute for Medical Research in Heidelberg and received his doctorate from the University of Göttingen in 1996. As a postdoc, Dr. Helmchen worked at the Bell Laboratories, Lucent Technologies, NJ. He then returned to the Max-Planck-Institute for Medical Research, Heidelberg, heading a junior research group from 2000–2005. In 2005, Dr. Helmchen was appointed Professor of Neurophysiology and Co-Director at the Brain Research Institute of the University of Zurich, Switzerland. His research is centered around the further development and application of imaging techniques for the study of neural network dynamics as basis of animal perception and behaviour.

Eric Seibel received undergraduate and master degrees in Mechanical Engineering from Cornell University and University of California, Berkeley, respectively. After working in the medical (ophthalmic) device industry, he designed and developed laser scanning microscopes for live tissue imaging for his doctorate from the University of Washington's Department of Bioengineering in 1996. Currently, Dr. Seibel is a Research Associate Professor in the Department of Mechanical Engineering, adjunct in Bioengineering and Electrical Engineering, and Director of the Human Photonics Lab at UW. His multidisciplinary research program develops and translates to industry novel technologies for optical scanning for image acquisition and display, with specific focus on the early detection and treatment of cancer and pre-cancer.

References

[1] E. J. Seibel, Optical Fibers and Sensors for Medical Diagnostics and Treatment Applications VIII, Proc. SPIE **6852**, 685207–685208 (2008).
[2] B. I. Hirschowitz, L. E. Curtiss, C. W. Peters, and H. M. Pollard, Gastroenterology **35**(1), 50; discussion 51–53 (1958).
[3] J. Baillie, Gastrointest. Endosc. **65(6)**, 886–893 (2007).
[4] Fujikura [FAI:Image Fiber] www.fujikura.com (2009).
[5] Sumitomo [Optical Fiber Bundle/Image Guide] http://www.sumitomoelectricusa.com (2009).
[6] M. A. Funovics, R. Weissleder, and U. Mahmood, Radiology **231**(3), 659–666 (2004).
[7] T. J. Muldoon, M. C. Pierce, D. L. Nida, M. D. Williams, A. Gillenwater, and R. Richards-Kortum, Opt. Exp. **15**(25), 16413–16423 (2007).
[8] J. A. Udovich, N. D. Kirkpatrick, A. Kano, A. Tanbakuchi, U. Utzinger, and A. F. Gmitro, Appl. Optics **47**(25), 4560–4568 (2008).
[9] J. Knittel, L. Schnieder, G. Buess, B. Messerschmidt, and T. Possner, Opt. Commun. **188**(5–6), 267–273 (2001).
[10] K. B. Sung, C. Liang, M. Descour, T. Collier, M. Follen, and R. Richards-Kortum, IEEE Trans. Biomed. Eng. **49**(10), 1168–1172 (2002).
[11] A. R. Rouse, A. Kano, J. A. Udovich, S. M. Kroto, and A. F. Gmitro, Appl. Optics **43**(31), 5763–5771 (2004).
[12] M. Oki, H. Saka, C. Kitagawa, C. Sako, S. Tanaka, Y. Kawada, and K. Mori, Chest **127**(6), 2271–2273 (2005).
[13] M. J. Suter, D. R. Riker, M. Mino-Kenudson, J. Thiesse, M. Rosenberg, K. A. Gallagher, M. Shishkov, B. E. Bouma, J. F. Beamis, and G. J. Tearney, Am. J. Resp. Crit. Care (submitted).
[14] Schott [SCHOTT North America – Image Bundle] www.us.schott.com (2009).
[15] C. W. Oyster, *The human eye structure and function,* Sinauer Associates, Inc., Sunderland, MA (1999).
[16] E. J. Seibel and Q. Y. J. Smithwick, Lasers Surg. Medic. **30**(3), 177–183 (2002).
[17] E. J. Seibel, Q. Y. J. Smithwick, C. M. Brown, and P. G. Reinhall, Biomonitoring and Endoscopy Technologies, Proc. SPIE **4158**, 29–39 (2001).
[18] E. J. Seibel, R. S. Johnston, and C. D. Melville, Optical Fibers and Sensors for Medical Diagnostics and Treatment Applications VI, Proc. SPIE **6083**, 608303–608308 (2006).

© 2010 by WILEY-VCH Verlag GmbH & Co. KGaA, Weinheim

[19] E. J. Seibel, C. M. Brown, J. A. Dominitz, and M. B. Kimmey, Gastrointest. Endosc. Clin. N. Am. **18**(3), 467–478 (2008).
[20] L. Giniunas, R. Juskaitis, and S. V. Shatalin, Appl. Optics **32**(16), 2888–2890 (1993).
[21] L. E. Kinsler, A. R. Frey, A. B. Coppens, and J. W. Sanders, *Fundamental of Acoustics*, John Wiley & Sons, New York (1982).
[22] W. Göbel, A. Nimmerjahn, and F. Helmchen, Opt. Lett. **29**(11), 1285–1287 (2004).
[23] C. J. Engelbrecht, R. S. Johnston, E. J. Seibel, and F. Helmchen, Opt. Exp. **16**(8), 5556–5564 (2008).
[24] Q. Y. J. Smithwick, P. G. Reinhall, J. Vagners, and E. J. Seibel, J. Dyn. Systems, Measure. Control **126**(1), 88–101 (2004).
[25] C. M. Brown, P. G. Reinhall, S. Karasawa, and E. J. Seibel, Opt. Eng. **45**(4), 043001-10 (2006).
[26] E. J. Seibel, C. M. Brown, M. J. Kundrat, and P. G. Reinhall, Proc. SPIE **5691**, 42–53 (2005).
[27] E. J. Seibel, R. E. Carroll, J. A. Dominitz, R. S. Johnston, C. D. Melville, C. M. Lee, S. M. Seitz, and M. B. Kimmey, IEEE Trans. Biomed. Eng. **55**(3), 1032–1042 (2008).
[28] Y. C. Wu, J. F. Xi, M. J. Cobb, and X. D. Li, Opt. Lett. **34**(7), 953–955 (2009).
[29] M. T. Myaing, D. J. MacDonald, and X. Li, Opt. Lett. **31**(8), 1076–1078 (2006).
[30] X. M. Liu, M. J. Cobb, Y. C. Chen, M. B. Kimmey, and X. D. Li, Opt. Lett. **29**(15), 1763–1765 (2004).
[31] E. Barhoum, R. Johnston, and E. Seibel, Opt. Exp. **13**(19), 7548–7562 (2005).
[32] L. Fu, X. S. Gan, and M. Gu, Opt. Exp. **13**(14), 5528–5534 (2005).
[33] C. J. Engelbrecht, W. Göbel, and F. Helmchen, Opt. Exp. **17**(8), 6421–6435 (2009).
[34] Q. Y. J. Smithwick and E. J. Seibel, Optical Biopsy IV, Proc. SPIE **4613**, 222–233 (2002).
[35] H. Haneishi, T. Ogura, and Y. Miyake, Opt. Lett. **19**(9), 601–603 (1994).
[36] K. Yao, Y. Takaki, T. Matsui, A. Iwashita, G. K. Anagnostopoulos, P. Kaye, and K. Ragunath, Gastrointest. Endosc. Clin. N Am. **18**(3), 415–433, (2008).
[37] E. J. Seibel, T. A. Brentnall, and J. A. Dominitz, Gastrointest. Endosc. Clin. N Am. **19**(2), 299–307 (2009).
[38] K. Berg, P. K. Selbo, A. Weyergang, A. Dietze, L. Prasmickaite, A. Bonsted, B. O. Engesaeter, E. Angell-Petersen, T. Warloe, N. Frandsen, and A. Hogset, J. Microsc. Oxford **218**, 133–147 (2005).
[39] E. J. Seibel, H. L. Kenerson, C. M. Lee, C. D. Melville, R. S. Johnston, and R. S. Yeung, Photodynamic Therapy: Back to the Future, Proc. SPIE **7380**, 73802A–8 (2009).
[40] J. T. C. Liu, M. W. Helms, M. J. Mandella, J. M. Crawford, G. S. Kino, and C. H. Contag, Biophys. J. **96**(6), 2405–2414 (2009).
[41] C. M. Lee, J. E. Chandler, and E. J. Seibel, Endoscopic Microscopic V, Proc. SPIE **7558**, 755806 (2010).
[42] V. V. Tuchin, *Handbook of optical biomedical diagnostics*, SPIE – The International Society for Optical Engineering, Bellingham, WA (2002).
[43] K. Badizadegan, V. Backman, C. W. Boone, C. P. Crum, R. R. Dasari, I. Georgakoudi, K. Keefe, K. Munger, S. M. Shapshay, E. E. Sheets, and M. S. Feld, Faraday Discuss. **126**, 265–279 (2004).
[44] H. Zeng, Y. S. Fawzy, M. A. Short, M. Tercelj, A. McWilliams, M. Petek, B. Palcic, J. Zhao, H. Lui, and S. Lam, Eng. Med. and Biology Society, 2008. EMBS 2008. 30th Annual International Conference of the IEEE, Proc., 1849–1850 (2008).
[45] A. Nijssen, S. Koljenovic, T. C. Bakker Schut, P. J. Caspers, and G. J. Puppels, J. Biophoton. **2**(1–2), 29–36 (2009).
[46] B. W. Tuttle and E. J. Seibel, Optical Fibers and Sensors for Medical Diagnostics and Treatment Applications VI, Proc. SPIE **6083**, 608307–608312 (2006).
[47] M. S. Yavuz, Y. Cheng, J. Chen, C. M. Cobley, Q. Zhang, M. Rycenga, J. Xie, C. Kim, K. H. Song, A. G. Schwartz, L. V. Wang, and Y. Xia, Nature Mater. **8**, 935–939 (2009).
[48] W. J. Yoon, S. Park, P. G. Reinhall, and E. J. Seibel, J. Med. Devices **3**(1), 011004–011009 (2009).
[49] T. D. Soper, D. R. Haynor, R. W. Glenny, and E. J. Seibel, Medical Imaging 2009: Visualization, Image-Guided Procedures, and Modeling, Proc. SPIE **7261**, 72610C–13 (2009).
[50] T. D. Soper, D. R. Haynor, R. W. Glenny, and E. J. Seibel, IEEE Trans. Biomed. Eng. **57**(3), 736–745 (2010).
[51] A. Osdoit, M. Genet, A. Perchant, S. Loiseau, B. Abrat, and F. Lacombe, Endoscopic Microscopy, Proc. SPIE **6082**, 608208–608210 (2006).
[52] F. Schwarz, A. Le Nevez, M. Genet, A. Osdoit, and F. Lacombe, Endoscopic Microscopy IV, Proc. SPIE **7172**, 71720G–11 (2009).
[53] Y. H. Tan and G. M. Preminger, Urol. Clin. N. Am. **31**(1), 33–42 (2004).
[54] A. S. Ross, and R. A. Kozarek, Curr. Opin. Gastroenterol. **25**(3), 245–51 (2009).
[55] D. Panescu, IEEE Eng. Med. Biol. Mag. **24**(4), 12–14 (2005).
[56] P. Swain, WORLD J. Gastroenterol. **14**(26), 4142–4145 (2008).
[57] D. L. Dickensheets and G. S. Kino, Opt. Lett. **21**(10), 764–766 (1996).
[58] D. L. Dickensheets and G. S. Kino, J. Microelectromech. Syst. **7**(1), 38–47 (1998).
[59] W. Piyawattanametha, H. Toshiyoshi, J. LaCosse, and M. C. Wu, Proc. Conference on Lasers and Electro-Optics, 2000 (CLEO 2000) 447–448 (2000).
[60] W. Piyawattanametha, R. P. Barretto, T. H. Ko, B. A. Flusberg, E. D. Cocker, H. Ra, D. Lee, O. Solgaard, and M. J. Schnitzer, Opt. Lett. **31**(13), 2018–2020 (2006).
[61] T. D. Wang, M. J. Mandella, C. H. Contag, and G. S. Kino, Opt. Lett. **28**(6), 414–416 (2003).
[62] H. Miyajima, K. Murakami, and M. Katashiro, IEEE J. Sel. Top. Quantum Electron. **10**(3), 514–527 (2004).
[63] J. R. Lewis, M. Holton, M. Kykta, A. Malik, F. Metting, C. Ryerson, C. Wiklof, and J. Xu, Proc. SPIE **5348**, 40–51 (2004).

© 2010 by WILEY-VCH Verlag GmbH & Co. KGaA, Weinheim

[64] L. Wu and H. Xie, Solid-State Sensors, Actuators and Microsystems Conference, 2009. TRANSDUCERS 2009. International, Proc., 2222–2225 (2009).
[65] D. L. Dickensheets and G. S. Kino, Three-Dimensional Microscopy: Image Acquisition and Processing, Proc. SPIE **2184**, 39–47 (1994).
[66] W. C. Wang, M. Fauver, J. N. Ho, E. J. Seibel, and P. G. Reinhall, Sens. Actuators A-Physical, **102**(1–2), 165–175 (2002).
[67] R. Kiesslich, J. Burg, M. Vieth, J. Gnaendiger, M. Enders, P. Delaney, A. Polglase, W. McLaren, D. Janell, S. Thomas, B. Nafe, P. R. Galle, and M. F. Neurath, Gastroenterology, **127**(3), 706–713 (2004).
[68] G. J. Tearney, S. A. Boppart, B. E. Bouma, M. E. Brezinski, N. J. Weissman, J. F. Southern, and J. G. Fujimoto, Opt. Lett. **21**(7), 543–545 (1996).
[69] D. Yelin, W. M. White, J. T. Motz, S. H. Yun, B. E. Bouma, and G. J. Tearney, Opt. Exp. **15**(5), 2432–2444 (2007).
[70] D. Yelin, B. E. Bouma, and G. J. Tearney, Opt. Exp. **16**(3), 1748–1757 (2008).
[71] D. Kang, D. Yelin, B. E. Bouma, and G. J. Tearney, Opt. Exp. **17**(17), 15239–15247 (2009).
[72] K. Goda, K. K. Tsia, and B. Jalali, Nature **458**(7242), 1145–1149 (2009).
[73] K. K. Tsia, K. Goda, D. Capewell, and B. Jalali, Opt. Lett. **34**(14), 2099–2101 (2009).
[74] D. Yelin, C. Boudoux, B. E. Bouma, and G. J. Tearney, Opt. Lett. **32**(9), 1102–1104 (2007).
[75] W. Göbel, J. N. Kerr, A. Nimmerjahn, and F. Helmchen, Opt. Lett. **29**(21), 2521–2523 (2004).
[76] K. L. Reichenbach, and C. Xu, Opt. Exp. **15**(5), 2151–2165 (2007).
[77] Y. K. Chen, Gastrointest. Endosc. **65**(2), 303–311 (2007).
[78] Y. K. Chen, and D. K. Pleskow, Gastrointest. Endosc. **65**(6), 832–841 (2007).
[79] K. Fife, A. El Gamal, and H. S. P. Wong, Electron Devices Meeting, 2007. IEDM 2007. IEEE International, Proc., 1003–1006 (2007).
[80] M. Cohen, F. Roy, D. Herault, Y. Cazaux, A. Gandolfi, J. P. Reynard, C. Cowache, E. Bruno, T. Girault, J. Vaillant, F. Barbier, Y. Sanchez, N. Hotellier, O. LeBorgne, C. Augier, A. Inard, T. Jagueneau, C. Zinck, J. Michailos, and E. Mazaleyrat, Electron Devices Meeting, 2006. IEDM '06. International, Proc., 1–4 (2006).
[81] M. Oda, T. Kaida, S. Izawa, T. Ogo, K. Itsumi, Y. Okada, and K. Sasada, Solid-State Circuits Conference, 2005. Digest of Technical Papers. Proc. ISSCC. 2005 IEEE International, **Vol. 1**, 346–602 (2005).
[82] F. Xiao, J. E. Farrell, and B. A. Wandell, Digital Photography, Proc. SPIE **5678**, 75–84 (2005).
[83] A. J. P. Theuwissen, Solid-State Electron. **52(9)**, 1401–1406 (2008).
[84] M. R. Billings, Foveon, Inc., USA (1998).
[85] B. E. Bayer, Eastman Kodak Company, USA(1975).
[86] P. M. Hubel, J. Liu, and R. J. Guttosch, Proc. SPIE **5301**, 402–407 (2004).
[87] Q. Y. J. Smithwick, J. Vagners, P. G. Reinhall, and E. J. Seibel, J. Dynam. Systems Meas. Control-Trans. ASME **128**(4), 899–913 (2006).
[88] Q. Y. J. Smithwick, J. Vagners, R. S. Johnston, and E. J. Seibel, J. Dynam. Systems Meas. Control-Trans. ASME **132**(1), (2010).
[89] S. G. Lipson, H. Lipson, and D. S. Tannhauser, *Optical Physics*, Cambridge University Press, Cambridge, 497 (1995).
[90] J. B. Pawley, *Handbook of Biological Confocal Microscopy*, Plenum Press, Chapter 33 (1995).
[91] E. J. Seibel, C. D. Melville, J. K. C. Lung, A. P. Babchanik, C. M. Lee, R. S. Johnston, and J. A. Dominitz, Medical Imaging 2009: Visualization, Image-Guided Procedures, and Modeling, Proc. SPIE **7261**, 72611C–7 (2009).
[92] P. Sharma, A. Bansal, S. Mathur, S. Wani, R. Cherian, D. McGregor, A. Higbee, S. Hall, and A. Weston, Gastrointest. Endosc. **64**(2), 167–175 (2006).
[93] O. S. Lin, D. B. Schembre, K. Mergener, W. Spaulding, N. Lomah, K. Ayub, J. J. Brandabur, J. Bredfeldt, F. Drennan, M. Gluck, G. C. Jiranek, S. E. McCormick, D. Patterson, and R. A. Kozarek, Gastrointest. Endosc. **65**(4), 577–583 (2007).
[94] F. C. Ramirez, M. S. Shaukat, M. A. Young, D. A. Johnson, and R. Akins, Gastrointest. Endosc. **61**(6), 741–746 (2005).
[95] G. J. T. Seok, H. Yun, B. J. Vakoc, M. Shishkov, Wang Y. Oh, A. E. Desjardins, M. J. Suter, R. C. Chan, J. A Evans, Ik-Kyung Jang, N. S. Nishioka, J. F. de Boer, and B. E. Bouma, Nature Medic. **12**(12), 1429–1433 (2006).
[96] B. C. Wilson, J. Biomed. Opt. **12**(5), 051401 (2007).
[97] R. E. Carroll and S. M. Seitz, Int. J. Comput. Vis. **85**(3), 307–315 (2009).
[98] E. J. Seibel, T. D. Soper, D. H. Haynor, and R. W. Glenny, Medimond, Tokyo, Japan, K330R9118, 143–149 (2008).
[99] F. Helmchen, Exp. Physiol. **87**(6), 737–45 (2002).
[100] B. A. Flusberg, J. C. Jung, E. D. Cocker, and M. J. Schnitzer, Biophys. J. **88**(1), 335a (2005).
[101] L. Fu, A. Jain, C. Cranfield, H. Xie, and M. Gu, J. Biomed. Opt. **12**(4), 040501 (2007).
[102] B. A. Wilt, L. D. Burns, E. T. Wei Ho, K. K. Ghosh, E. A. Mukamel, and M. J. Schnitzer, Annu. Rev. Neurosci. **32**, 435–506 (2009).
[103] F. Helmchen, M. S. Fee, D. W. Tank, and W. Denk, Neuron, **31(6)**, 903–912 (2001).
[104] B. A. Flusberg, J. C. Jung, E. D. Cocker, E. P. Anderson, and M. J. Schnitzer, Opt. Lett. **30**(17), 2272–2274 (2005).
[105] B. A. Flusberg, A. Nimmerjahn, E. D. Cocker, E. A. Mukamel, R. P. Barretto, T. H. Ko, L. D. Burns, J. C. Jung, and M. J. Schnitzer, Nature Meth. **5**(11), 935–938 (2008).
[106] W. Piyawattanametha, E. D. Cocker, L. D. Burns, R. P. Barretto, J. C. Jung, H. Ra, O. Solgaard, and M. J. Schnitzer, Opt. Lett. **34**(15), 2309–2311 (2009).
[107] W. Denk, J. H. Strickler, and W. W. Webb, Science **248**(4951), 73–6 (1990).

© 2010 by WILEY-VCH Verlag GmbH & Co. KGaA, Weinheim

[108] W. Denk and K. Svoboda, Neuron **18**(3), 351–7 (1997).
[109] F. Helmchen and W. Denk, Nature Meth. **2**(12), 932–940 (2005).
[110] D. G. Ouzounov, K. D. Moll, M. A. Foster, W. R. Zipfel, W. W. Webb, and A. L. Gaeta, Opt. Lett. **27**(17), 1513–1515 (2002).
[111] F. Helmchen, D. W. Tank, and W. Denk, Appl. Optics **41**(15), 2930–2934 (2002).
[112] J. Sawinski and W. Denk, J. Appl. Phys. **102**(3), 034701 (2007).
[113] L. Fu, A. Jain, H. Xie, C. Cranfield, and M. Gu, Opt. Exp. **14**(3), 1027–1032 (2006).
[114] S. Tang, W. Jung, D. McCormick, T. Xie, J. Su, Y. C. Ahn, B. J. Tromberg, and Z. Chen, J. Biomed. Opt. **14**(3), 034005 (2009).
[115] J. C. Jung and M. J. Schnitzer, Opt. Lett. **28**(11), 902–904 (2003).
[116] L. Fu and M. Gu, Opt. Lett. **31**(10), 1471–3 (2006).
[117] Y. Wu, Y. Leng, J. Xi, and X. Li, Opt. Exp. **17**(10), 7907–7915 (2009).
[118] R. S. Johnston and E. J. Seibel, Scanning *fiber endoscope prototype performance*, Optical Society of America, Rochester, NY (2004).
[119] B. Messerschmidt, A. Kraeplin, S. Schenkl, I. Riemann, M. Stark, A. Ehlers, A. Tchernook, R. Le Harzic, and K. Koenig, Endoscopic Microscopy II, Proc. SPIE **6432**, 643202 (2007).
[120] H. Bao and M. Gu, Opt. Exp. **17**(12), 10098–10104 (2009).
[121] J. Sawinski, D. J. Wallace, D. S. Greenberg, S. Grossmann, W. Denk, and J. N. D. Kerr, PNAS **106**(46), 19557–19562 (2009).
[122] I. Veilleux, M. Doucet, P. Cote, S. Verreault, M. Fortin, P. Paradis, S. Leclair, R. S. D. Costa, B. C. Wilson, E. J. Seibel, O. Mermut, and J.-F. Cormier, Proc. SPIE **7558**, 75580D (2010).

© 2010 by WILEY-VCH Verlag GmbH & Co. KGaA, Weinheim